Earth-Science Reviews 240 (2023) 104399

Contents lists available at ScienceDirect

Earth-Science Reviews

journal homepage: www.elsevier.com/locate/earscirev

A review of plagioclase growth rate and compositional evolution in mafic alkaline magmas: Guidelines for thermometry, hygrometry, and timescales of magma dynamics at Stromboli and Mt. Etna

P. Moschini [a,*], S. Mollo [a,b], A. Pontesilli [b], M. Nazzari [b], C.M. Petrone [c], S. Fanara [d], A. Vona [e], M. Gaeta [a], C. Romano [e], P. Scarlato [b]

[a] Department of Earth Sciences, Sapienza - University of Rome, P. le Aldo Moro 5, 00185 Roma, Italy
[b] Istituto Nazionale di Geofisica e Vulcanologia - Department Roma 1, Via di Vigna Murata 605, 00143 Roma, Italy
[c] The Natural History Museum, Department of Earth Sciences, Cromwell Road, SW7 5BD London, United Kingdom
[d] Abteilung Experimentelle und Angewandte Mineralogie, Georg August Universität Göttingen, Goldschmidtstraße 1, 37077 Göttingen, Germany
[e] Dipartimento di Scienze, Università degli Studi Roma Tre, L.go San Leonardo Murialdo 1, 00146 Roma, Italy

ARTICLE INFO

Keywords:
Mafic alkaline magmas
Plagioclase growth rate parameterization
Plagioclase-based thermometry and hygrometry

ABSTRACT

Mafic alkaline magmas, such as those feeding the persistent eruptive activity of Stromboli and Mt. Etna volcanoes in Italy, are dominated by the crystallization of plagioclase via cooling and degassing phenomena related to the dynamics of shallow crustal reservoirs and eruptive conduits. Because plagioclase textures and compositions are extremely sensitive to the changes of intensive variables in subvolcanic plumbing systems, the phenomenological variability of erupted crystals preserves detailed evidence of complex growth histories. From this point of view, we reappraise the textural maturation and compositional complexity of plagioclase by allying thermodynamic and kinetic principles to natural and experimental observations, with the purpose of drawing up guidelines for reconstructing magma dynamics in mafic alkaline volcanic settings. A multifaceted statistical method is adopted to parameterize the decay of crystal growth rate with increasing crystallization time, as relaxation kinetics prevails over melt supersaturation effects. This model parameterization is combined with the textural analysis of natural plagioclase crystals to quantify the residence time of phenocrysts in equilibrium with magmas at Stromboli and Mt. Etna and/or the timescale of rapid microlite growth during disequilibrium ascent of magmas within the conduit. The role played by temperature and melt-water content on plagioclase components and major cation substitution mechanisms is also evaluated under both isobaric-isothermal and decompression conditions. The emerging paradigm is that the influence of dissolved water on anorthite-albite exchange between plagioclase and melt is overwhelmingly mitigated by changes in temperature at conditions of P = 30–300 MPa, T = 1050–1150 °C, fO_2 = NNO + 1.9-NNO + 2.3, and melt-H_2O = 0.6–4.4 wt%. As a corollary, anorthite and albite melt activities are almost fully encapsulated in the variation of anhydrous melt components as the crystallization of plagioclase proceeds during magma cooling. Following this line of reasoning, we propose an integrated modeling approach to decipher complex zoning patterns in natural plagioclase phenocrysts from mafic alkaline eruptions. Key findings from our re-assessment of equilibrium, thermometric, and hygrometric models indicate that temperature and dissolved water can be iteratively estimated for different plagioclase textural patterns if crystals are sufficiently strongly zoned and probability-based criteria are applied to determine the maximum probability distribution from kernel density analysis.

1. Introduction

Textural and compositional variations of plagioclase are profoundly controlled by plumbing system and conduit dynamics (e.g., Giacomoni et al., 2014; Arzilli et al., 2019). Plagioclase morphological evolution contributes to a plethora of textural terminologies associated with different magma crystallization conditions (e.g., equant, faceted, tabular, cellular, acicular, hopper, dendritic, skeletal, swallowtail,

* Corresponding author at: Department of Earth Sciences, Sapienza - University of Rome, P. le Aldo Moro 5, 00185 Roma, Italy.
E-mail address: piergiorgio.moschini@uniroma1.it (P. Moschini).

https://doi.org/10.1016/j.earscirev.2023.104399
Received 24 May 2022; Received in revised form 20 March 2023; Accepted 24 March 2023
Available online 26 March 2023

dusty, spongy, patchy, honeycomb, sieved, etc.; Singer et al., 1993; Hammer and Rutherford, 2002). In the ideal formula of plagioclase (MT_4O_8), cations are ordered in both tetrahedral (T) and octahedral (M) sites, thus forming two characteristic end-members: anorthite ($CaAl_2Si_2O_8$; An) and albite ($NaAlSi_3O_8$; Ab). Intracrystalline heterogeneities in plagioclase are generally described as grading An chemical variations or alternating An-rich and An-poor zones, which are categorized as normal zoning, reverse zoning, concentric zoning, oscillatory zoning, and sector zoning (Smith and Lofgren, 1983).

Different crystal habits and zoning patterns reflect changes in temperature (cooling) and melt-water content (decompression) during convective stirring (Couch et al., 2001) or ascent of magma towards shallower crustal reservoirs (Couch et al., 2003; Brugger and Hammer, 2010; Del Gaudio et al., 2010; Mollo et al., 2011; Iezzi et al., 2014). Plagioclase preserves evidence of extensive dissolution and recrystallization reactions associated with inputs of hot, water-poor (Cassidy et al., 2016) or water-rich (Cashman and Blundy, 2013) magmas from depth. The saturation temperature of plagioclase may also increase with increasing magma crystallinity as the result of latent heat release during exothermic, decompression-driven crystallization of water-saturated melts (Couch et al., 2003; Blundy et al., 2006).

According to the processes illustrated above, plagioclase is acknowledged as a powerful recorder of the physio-chemical conditions controlling the differentiation of magma and its crystallization history (Putirka, 2008; Humphreys et al., 2016; Pontesilli et al., 2021). Several efforts have been made by authors for interrogating plagioclase textures and compositions in terms of crystal growth dynamics (Cashman, 1993; Agostini et al., 2013; Vona and Romano, 2013; Andrews, 2021), cation partitioning (Dohmen and Blundy, 2014; Sun et al., 2017), equilibrium components (Ghiorso and Carmichael, 1980; Glazner, 1984; Putirka, 2005; Namur et al., 2012), thermodynamic, thermometric, and hygrometric modeling (Ghiorso and Carmichael, 1980; Glazner, 1984; Housh and Luhr, 1991; Lange et al., 2009; Putirka, 2005, 2008, 2017; Waters and Lange, 2015; Huggins et al., 2021). The free energy difference between crystal and melt is also responsible for the stability and morphological evolution of plagioclase under cooling and/or decompression-degassing crystallization regimes controlling subvolcanic plumbing system dynamics (Hammer and Rutherford, 2002; Arzilli et al., 2019). In this scenario, reaction kinetics related to the total free energy change of the system are inhibited by the prevailing control of relaxation phenomena on cation equilibrium partitioning as the plagioclase-melt interface approaches equilibrium at lower degrees of undercooling (Mollo et al., 2011; Mollo and Hammer, 2017).

Particular attention is given in this review study to the parameterization of crystal growth kinetics and the modeling of plagioclase equilibrium composition and temperature during solidification of mafic alkaline magmas, such as those typifying the present-day activity at Stromboli and Mt. Etna, two of the most active and monitored volcanoes in Italy and in the world (e.g., La Spina et al., 2016; Di Stefano et al., 2020). Upon identifying disparate aspects of plagioclase growth scenarios, we integrate experimental and natural data from literature with an internally consistent data set retrieved for mafic to intermediate magmas. Plagioclase textural and compositional parameters are comparatively examined under the rationale of thermodynamic and kinetic principles. This approach is pivotal to track the temporal scales of magma dynamics via plagioclase growth histories, as well as to disambiguate the role of temperature and melt-water content on plagioclase zoning patterns at Stromboli and Mt. Etna. Our final purpose is to provide a comprehensive background for future investigations, as well as informative guidelines and a secure methodology to model pre- and *syn*-eruptive conditions in active volcanic settings.

2. Methods

For the purpose of this study, we present here an internally consistent data set consisting of seventy-two new experiments carried out using two mafic alkaline basalts erupted at Mt. Etna (i.e., Monte Maletto Formation dated ~7 kyr ago) and Stromboli (i.e., 3 July 2019 paroxysm) as natural starting materials.

2.1. Experimental procedure

The powdered rocks are melted to ensure homogeneity at the HP-HT Laboratory of Experimental Volcanology and Geophysics of the Istituto Nazionale di Geofisica e Vulcanologia (INGV), Rome, Italy. A crucible containing the natural powder is loaded in a 1 atm vertical tube $CO–CO_2$ gas-mixing furnace at 1300 °C for 1 h. The redox state is 2 log unit above the Ni-NiO buffer (NNO + 2), comparable to the oxygen fugacity estimated at Mt. Etna (Mollo et al., 2015a) and Stromboli (Di Stefano et al., 2020). Iron loss is kept to <5% of the initial amount by adopting a Fe pre-saturated Pt crucible. Quenched glasses are analyzed by scanning electron microscopy and no crystalline phases are detected. Averages of twenty microprobe analyses of different glass chips for Mt. Etna and Stromboli are reported in Supplementary Material 1.

Isothermal-isobaric and decompression experiments are carried out in an internally heated pressure vessel (IHPV) equipped with a continuum decompression system and a rapid quenching device (drop quench) at the Abteilung Experimentelle und Angewandte Mineralogie, Georg August Universität Göttingen in Germany (Supplementary Material 1). Powdered starting glasses are loaded in Fe-presaturated Pt-capsules (e.g., Gaetani and Grove, 1998). Isothermal-isobaric experiments are conducted at 300 MPa and 1150, 1125, 1100, 1075, and 1050 °C. These experimental conditions reproduce most of magma crystallization paths at Mt. Etna (Mollo et al., 2015a) and Stromboli (Di Stefano et al., 2020). Experiments are heated directly to the target temperature at a rate of 50 °C/min and then the temperature is kept constant for ~23–27 h. No superliquidus pretreatment is imposed to the experimental charge and the system relaxes towards equilibrium as temperature and pressure are kept constant over the experimental time (cf. Moschini et al., 2021). Decompression experiments are conducted at the same temperatures of isothermal-isobaric runs by depressurizing the charges from 300 to 30 MPa at slow (0.018 MPa s^{-1}) and fast (0.98 MPa s^{-1}) rates over experimental times of ~4 h and ~ 5 min, respectively (Supplementary Material 1). Depressurization rates are selected in conformity with magma ascent velocities in the upper crust (0.45–24.5 m s^{-1}), as reported in geophysical, petrological, and numerical studies on Mt. Etna and Stromboli (Aloisi et al., 2006; Mollo et al., 2015b; La Spina et al., 2016, 2021; Polacci et al., 2019; Moschini et al., 2021). Water solubility in the mafic alkaline basalts is ~3 wt% at 300 MPa under isothermal-isobaric equilibrium, whereas disequilibrium degassing due to melt decompression results in volatile supersaturation and kinetic melt-fluid fractionation (Mollo et al., 2017). On this basis, deionized water (up to ~5 wt%) and oxalic acid (~0.2 wt% CO_2 by thermal decomposition) are added to the starting materials to attain both fluid-absent and fluid-present crystallization conditions (Supplementary Material 1). Plagioclase liquidus is independent of P_{H2O} under fluid-absent crystallization conditions. Conversely, under fluid-present crystallization conditions, plagioclase liquidus is controlled by volatile exsolution that imposes an actual undercooling variable of 14 to 30 °C (Moschini et al., 2021). Undercooling is regarded as the difference between the system temperature and the temperature at which a mineral phase saturates in the given liquid (Kirkpatrick, 1981). The degree of undercooling is associated with either a decrease in temperature or compositionally-induced increase of melt's liquidus temperature by decompression under H_2O-saturated conditions. The term actual undercooling is used to distinguish the driving force caused by compositional change from that of temperature change, as reported in Mollo and Hammer (2017). In both cases, the actual undercooling is quantified by the difference between the phase-in and system temperatures. In our decompression experiments, plagioclase liquidus as a function of P_{H2O} and T has been determined by Moschini et al. (2021) using the MELTS code (*v*.1.2.0; Gualda et al., 2012). The experimental temperature is monitored by three S-type

(Pt90Rh10/Pt with uncertainty of ±3 °C) thermocouples and pressure is recorded by a transducer, calibrated against a Heise tube gauge with accuracy ±5 MPa. Experiments are quenched using a drop quench device imposing a cooling rate of ~150 °C s^{-1}. The use of Ar as a pressure medium provided an intrinsic fO_2 variable from NNO + 2 to NNO + 4 (Schanofsky et al., 2019). Within the sample capsule, fH_2 is controlled by hydrogen permeation through the capsule walls driven by the fugacity gradient between the pressure medium and the capsule interior. Hydrogen permeation determined the fO_2 inside the capsule through the equilibrium: $H_2 + 1/2\ O_2 \leftrightarrow H_2O$. However, under fluid-present conditions and with the addition of CO_2, the redox state of the system changes in response to the variable activity of water in the melt (Botcharnikov et al., 2008). Under such conditions, a more accurate fO_2 estimate is obtained at the end of experimental runs through the oxygen barometer of Ishibashi (2013) that is based on spinel–melt equilibria in alkaline systems, with uncertainty ±0.3 log unit. This model returns fO_2 estimates variable from NNO + 1.9 and NNO + 2.3 buffer, as reported in Moschini et al. (2021).

2.2. Microchemical analysis

Major element concentrations are obtained at the HP-HT Lab of INGV using a JEOL-JXA8200 electron probe micro-analyzer (EPMA) equipped with five wavelength dispersive spectrometers (Supplementary Material 2). For glasses, a slightly defocused 5 μm beam is used with a counting time of 5 s on background and 15 s on peak. For crystals, beam size is 1 μm with a counting time of 20 and 10 s on peak and background, respectively. The analytical conditions are 15 kV accelerating voltage and 10 nA beam current. The following standards are used for calibration: jadeite (Si and Na), corundum (Al), forsterite (Mg), andradite (Fe), rutile (Ti), orthoclase (K), apatite (P), and spessartine (Mn). Sodium and potassium are analyzed first to prevent alkali migration effects. Counting statistics are used to determine precision for each element on each analysis, whereas the secondary standards are used to determine the accuracy. Precision and accuracy are found to be better than 5% for all cations.

Raman spectra are acquired at EVPLab of Roma Tre University (Rome, Italy) using a Jobin Yvon LABRAM HR800 Horiba micro-Raman spectrometer, equipped with an attenuated doubled Nd3:YAG laser (532 nm wavelength) and calibrated using a silicon standard. The operating conditions are 600 grooves/mm grating density, confocal hole opening 300 μm, and slit aperture 200 μm, exposure time of 60 s (3 times). The laser power at source is 60 mW (0.15 mW on the sample surface). A nominal spatial resolution of ~5 μm^2 is obtained with the 100× objective. For each sample, 5 spectra are acquired to assess data reproducibility. The backscattered Raman radiation is collected over ranges of 100–1500 cm^{-1} and 2700–4000 cm^{-1}, corresponding to low-wavenumber (*LW*) silicate and high-wavenumber (*HW*) water regions, respectively. The Matlab© code developed by Di Genova et al. (2017) is used to perform Long correction (Long, 1977), background subtraction, and *HW/LW* parameterization (i.e., Raman band area ratio). For the quantification of melt-water content, Raman spectra are standardized against a set of well characterized glasses with mafic alkaline compositions (see Mollo et al., 2017). Their water contents are independently determined by Fourier transform infrared spectroscopy (FTIR) and Karl Fischer titration (KFT). Raman data and calibration fit [$(HW/LW)_{Raman}$ against $H_2O_{Standard}$] are reported in Supplementary Material 3.

2.3. Textural analysis

Photomicrographs are collected in backscattered electron (BSE) mode with a JEOL 6500F field emission gun scanning electron microscope (FE-SEM) equipped with an energy-dispersive spectrometer (EDS) detector at the HP-HT Lab of INGV. The acquired photomicrographs are processed using NIH ImageJ software and reduced to binary images (i.e., black and white color) by grey level thresholding (i.e., image segmentation). The uncertainty associated with the segmentation process is evaluated by adding/subtracting pixel layers around each crystal in the binary image (cf. Pontesilli et al., 2019). Error propagation analysis yields an uncertainty of 30% for the determination of plagioclase growth rate. The Matlab© code designed by Moschini et al. (2021) is used to perform image processing operations and measure equal-area best-fit ellipses and lengths of major (*L* in mm) and minor (*W* in mm) axes. Following Armienti et al. (1994) and Armienti (2008), crystals with $L < 0.006$ mm are considered artefacts produced by image segmentation analysis carried out with NIH ImageJ software and are removed from the data set, together with crystal fragments at the edge of photomicrographs.

Crystal size distribution (CSD) analysis is carried out through *CSDCorrections* 1.38 (Higgins, 2000) to determine binned curves sorted in different crystal size classes. Intersection planar data are converted into volume data by applying stereological correction to retrieve the actual distribution of crystal sizes from the measured population of intersections (Higgins, 2000). This correction method accounts for 1) potential cut-section effects in the case of larger crystals cut by a plane shifted with respect to the center, therefore contributing to smaller crystal populations; and 2) intersection probability effects when, for a poly-disperse distribution, smaller crystals are less likely to be intersected by a plane than larger crystals (Higgins, 2000). The crystal aspect ratio (*L/W*) is determined by *CSDslice* (Morgan and Jerram, 2006), in which 2D raw data are compared with a crystal habit database to constrain the five best-matching 3D crystal shapes. CSD diagrams are in the form of semi-logarithmic ln*N(L)* against *L* plots (Marsh, 1988):

$$lnN(L) = \frac{-L}{G\,\tau} + lnN_0 \quad (1)$$

where *N(L)* is the number of crystals per unit length per unit volume (i.e., the density distribution of crystals per unit volume per bin size), *G* is the crystal growth rate, τ is the steady-state crystallization time, and N_0 is the nucleation density (i.e., the number of crystals of zero size). The linear regression fit of a CSD curve has slope $m = 1 / (G \times \tau)$ and intercept $b = \ln(N_0)$.

Knowing that τ from classical CSD theory can be rewritten as *t*, the volumetric growth rate of plagioclase for the mean area investigated is calculated through the formulation:

$$G = (L\,W)^{0.5} \Big/ (2\,t) \quad (2)$$

where the factor ½ accounts for the growth of crystals in both directions. *L* and *W* are measured as the average of ten largest crystals and their incorporation in Eq. (2) has the virtue of minimizing the uncertainty related to crystal size classification and quantification, also increasing the probabilities to intersect the true maximum L. Moreover, crystal inequidimensionality and sectioning artefacts related to crystal cuts are mediated over both major and minor lengths (Fenn, 1977; Swanson, 1977).

2.4. Statistical analysis

Through the statistical algorithm of Statgraphics Centurion 18® (Statpoint Technologies, Inc., Warrenton, VA, USA), we perform multivariate regression analysis among different variables to determine the *p-value*. This is an important metric for identifying the best subset of independent *n* variables relative to a selected target variable. The *p-value* is a probability number describing the likelihood that the data distribution occurs under the null hypothesis. If the null hypothesis is true, an independent *n* variable has no significant effect over the target variable. If the null hypothesis is rejected, the alternate hypothesis is that the independent *n* variable has a significant effect on the target variable. A *p-value* < 0.05 is assumed as a statistically significant result, which implies that the null hypothesis should be rejected. In conjunction with *p-value*,

the product moment correlation coefficient *Pearson's r* is derived from the correlation matrix to quantify the strength of correlation among *n* variables. Statistical significance of *Pearson's* $r = \pm 1$ is equivalent to $\pm 1^2 \times 100 = 100\%$ of correlation, whose magnitude ranges between -1 (highest negative correlation) and $+1$ (highest positive correlation). *Pearson's r* from a correlation matrix is proportional to the standardized regression coefficient *I* derived by multiple linear regression analysis. *I* in percentage represents the influence exerted by independent *n* variables on the target variable, calculated as the unstandardized regression coefficient of the independent variable multiplied by its standard deviation and divided by the standard deviation of the target variable. To test if regression variables are indeed independent or, alternatively, are highly correlated providing unreliable regression statistics (i.e., multicollinearity), the variance inflation factor (*VIF*) is employed. *VIF* quantifies how much the variance of a coefficient is inflated because of linear dependence with other regression variables and values exceeding 10 are often regarded as indicating multicollinearity (Hair et al., 1995).

Multiple linear regression analysis is adopted in this study to develop and test different models. With this approach some independent variables may closely describe the variance of the data, whereas some others may generate a set of predictions with low degrees of freedom that lead to data overfitting. We identify and remove variables that do not improve the fit by using an a priori correlation matrix and assume those with *p-value* ≥ 0.05, *Pearson's* $r \leq 0.60$ (as absolute value), and *VIF* > 10 as unsuitable predictors. Among all the remaining filtered predictors, we select the best independent variables for the model through the *Mallows' Cp* statistic. This parameter is expressed as $RSS_k/RSS_p - n + 2p$, where RSS_k is the ratio of the residual sum of squares of all predictors *k*, RSS_p is the residual sum of squares of only *p* of the *k* predictors, and *n* is the number of observations. *Mallows' Cp* is a measure of the bias in a model: if the type and number of selected predictors *p* (including the constant term in linear regression) are sufficient to provide a good description of the data, then *Cp* has values as close as possible to *p*. The accuracy of the calibrated model is verified as follows: 1) ~20% of data are randomly subtracted from the data set before the regression analysis, 2) the remaining ~80% of the data are regressed to derive a preliminary model, 3) subtracted data are used as test data for the preliminary model, and 4) the whole data set is regressed to calculate the overall predictive model. Regression statistics associated with these calculations are the coefficient of determination (R^2), standard error of estimate (*SEE*), and average absolute deviation (*AAD*).

3. Plagioclase growth rate parameterization

3.1. Plagioclase growth principles

The crystal growth process is strictly related to crystal-melt interface kinetics resulting from the attachment/detachment of cations to the advancing crystal interface and the diffusion of chemical components in the liquid (Jackson, 1969; Dowty, 1980; Kirkpatrick, 1981; Cashman, 1990; Lasaga, 1998; Hammer, 2008; Mollo and Hammer, 2017). Attainment of bulk thermodynamic equilibrium (i.e., a minimum energy state) at the crystal-melt interface corresponds to a time-independent steady-state crystallization condition at which the crystal growth is halted (Tsuchiyama, 1983). Because crystallization is an exothermic process, the crystal growth rate depends on the temperature at which interface kinetics develop. Hence, a certain degree of undercooling is essential to promote the growth and textural maturation of crystals (Kirkpatrick, 1981). For a small degree of undercooling, the crystal growth rate initially increases towards a maximum corresponding to a small energetic barrier to overcome for the attachment of atoms on the advancing plagioclase surface (Kirkpatrick et al., 1979; Muncill and Lasaga, 1987). However, as the degree of undercooling increases, the crystal growth rate does not further increase but rather decreases, as the activation energy for cation attachment onto the plagioclase surface becomes prohibitively large (Kirkpatrick et al., 1979; Muncill and Lasaga, 1987).

Interface kinetics resulting from a large degree of undercooling lead to development of diffusive boundary layers in the melt next to the advancing plagioclase surfaces (Lofgren, 1980). Under such condition, the solidifying system shifts from an interface-controlled crystallization regime to a diffusion-controlled regime (Hammer and Rutherford, 2002; Couch et al., 2003). Imbalance between crystal growth rate and diffusion of cations in the melt implies that the compositional difference between diffusive and far field melt is proportional to the degree of undercooling (Tsuchiyama, 1983, 1985; Mollo et al., 2011). Therefore, in a supersaturated melt, the driving force of undercooling for the crystal growth approximates to supersaturation gradients arising from concentration-dependent reactions induced by interface kinetics (Tsuchiyama, 1983, 1985; Mollo et al., 2011). In other words, both the effects of supersaturation and undercooling are imputable to the same process, as outlined by Kirkpatrick (1981). Moreover, the crystal growth rate approaches zero as diffusion gradients in the melt decrease over time and the system relaxes towards equilibrium, in response to a minimum free energy difference between crystal and melt.

Initial supersaturation effects and compositional heterogeneities at the interface melt are counterbalanced by relaxation phenomena that become more effective over the timescale of crystallization (Hammer, 2008). Relaxation kinetics lower the concentration gradients at the crystal-melt interface and favor a steady-state textural maturation of crystals, with development of euhedral forms (Kirkpatrick, 1975). As a consequence, the crystal growth is not always linear in the early stages of crystallization and plagioclase may take time for the establishment of equilibrium texture, a condition at which the growth rate goes to zero (Nabelek et al., 1978). An important consequence of melt relaxation is that the crystal growth rate of plagioclase progressively decreases with increasing crystallization time until bulk chemical gradients cease, and the interface melt returns to homogeneous concentrations (Grove, 1978; Cashman, 1993; Kohut and Nielsen, 2004; Hammer, 2008). Near-equilibrium crystallization conditions are restored when the effect of interface kinetics becomes small and attachment/detachment reactions of cations from the melt onto the crystalline surface (and vice versa) occur at comparable rate (Pontesilli et al., 2019).

Because the effect of undercooling and the mobility of melt components are interdependent, crystal growth rate changes as a function of melt composition and viscosity (Zhang, 2010; Vetere et al., 2015). In silicate melts, the energetic barrier to overcome for the onset of nucleation roughly scales with the proportion of tetrahedral relative to octahedra sites, which corresponds to the degree of melt polymerization (Naney and Swanson, 1980; Kirkpatrick, 1983). The internal structure of silicate melt can be assumed as an equilibrium arrangement of silicon-oxygen-metal bonds, in terms of bond lengths and strengths (Bottinga and Weill, 1972). For each subliquidus temperature, a specific equilibrium internal structure must be attained by the melt to nucleate a stable crystalline phase. The effect of undercooling determines a rearrangement of the melt internal structure, which progressively attains a new equilibrium state over a certain time. This temporal interval is defined as incubation time (or lag time) and corresponds to a delay in the crystallization of mineral phases from structurally unrelaxed melts (Swanson, 1977; Tsuchiyama, 1983; Hammer, 2008). In more polymerized melts, the number of oxygens bonded to two tetrahedrally coordinated cations (i.e., bridging oxygens *BO*) increases, whereas the number of oxygens bonded to a tetrahedrally coordinated cation and to a different cation in another coordination state (i.e., non-bridging oxygens *NBO*) decreases. The parameter NBO/T^{melt}, defined as to the number of *NBO* per tetrahedrally coordinated cations *T,* is used to quantify melt structural changes as a function of compositional variations (Mysen et al., 1985). As the degree of undercooling increases, melts with low NBO/T^{melt} are less inclined to crystallize than those with high NBO/T^{melt} and, comparatively, Si—O rich crystals appear more delayed than Si—O poor ones (Iezzi et al., 2011).

Dissolved H_2O also controls the melt structure and viscosity, by

producing more depolymerized melts with dramatic effects on the nucleation density and growth rate of plagioclase, as described in Fenn (1977). According to this proposition, the growth rate of plagioclase is observed to decrease with increasing the amount of albite relative to anorthite components in the melt phase (Kirkpatrick et al., 1979, 1983; Muncill and Lasaga, 1987). Moreover, owing to the difference in bonding energy between Si—O (443 kJ mol^{-1}) and Al—O (330–422 kJ mol^{-1}), the transfer of Al^{3+} cations from the melt to the surface of a rapidly growing plagioclase crystal is more facilitated than the transfer of Si^{4+} cations (Iezzi et al., 2011). As a consequence, under cooling-induced crystallization regimes, Ab-rich plagioclase crystals are delayed relative to An-rich ones, such as the delay time increases with increasing undercooling (Mollo et al., 2011, 2012; Iezzi et al., 2014). An opposite effect is documented under decompression-induced crystallization regimes where undercooling is governed by the exsolution of water from the melt (Pupier et al., 2008; Crabtree and Lange, 2011; Waters and Lange, 2015). A progressive decrease of water concentration dissolved in the melt rises the liquidus-solidus loop of plagioclase for the Ab-An system by changing its topology and enlarging the stability of low-temperature sodic end-member relative to the high-temperature calcic one. The composition plagioclase resulting from more degassed and undercooled melts becomes preferentially enriched in Ab and depleted in An components (Pupier et al., 2008; Crabtree and Lange, 2011; Waters and Lange, 2015).

3.2. Growth-related plagioclase parameters

The textural change of plagioclase from isobaric-isothermal and decompression experiments from this study and carried out on Mt. Etna and Stromboli mafic alkaline melts conforms to previous observations reported in a plethora of experimental and natural studies investigating basaltic to rhyolitic terrestrial rocks and lunar samples (Moore and Evans, 1967; Lofgren, 1974; Ikeda, 1977; Swanson, 1977; Wright and Okamura, 1977; Grove, 1978; Nabelek et al., 1978; Corrigan, 1982; Kouchi et al., 1986; Shirley, 1987; Muncill and Lasaga, 1987, 1988; Grove, 1990; Kirkpatrick, 1981; Hammer and Rutherford, 2002; Cashman and Marsh, 1988; Kneedler, 1989; Cashman, 1990, 1993; Cashman et al., 1999; Burkhard, 2002, 2005a, 2005b; Couch, 2003; Couch et al., 2003; Kohut and Nielsen, 2004; Simakin and Salova, 2004; Larsen, 2005; Conte et al., 2006; Hammer, 2008; Orlando et al., 2008; Pupier et al., 2008; Schiavi et al., 2009, 2010; Brugger and Hammer, 2010; Crabtree and Lange, 2011; Mollo et al., 2011; Mollard et al., 2012; Agostini et al., 2013; Iezzi et al., 2011, 2014; Shea and Hammer, 2013; Arzilli et al., 2019; Giuliani et al., 2020; Le Gall et al., 2021). We will not reiterate here the textural evolution of plagioclase under interface-controlled and diffusion-controlled growth regimes but rather point to the primary motivation of our experiments, which is the parameterization of plagioclase growth rate in mafic systems.

In short, the mineral phase assemblage of our experiments consists of plagioclase + clinopyroxene ± titanomagnetite (Supplementary Material 1), as already documented in previous experimental works on Stromboli (Agostini et al., 2013 and references therein) and Mt. Etna (Mollo et al., 2018 and references therein). The aspect ratio of plagioclase is observed to change from ≤7 (blocky, prismatic, and tabular) to ≥11 (elongate and acicular) from isothermal-isobaric to decompression conditions (Supplementary Material 1). As the depressurization rate increases, the plagioclase growth rate expressed on a logarithmic scale increases from −14 to −8 mm s^{-1} (Fig. 1a). According to Couch et al. (2003), interface kinetics favors the onset of plagioclase crystals with larger sizes and higher aspect ratios (Supplementary Material 1). Much slower growth rates from −16 to −15 mm s^{-1} are measured for smaller plagioclase crystals obtained from isobaric-isothermal experiments (Fig. 1a). Under these conditions, plagioclase growth is hindered by sluggish kinetic effects resulting from minimum free energy difference between melt and crystal (Hammer and Rutherford, 2002; Hammer, 2008). The growth rate sightly increases with increasing the system

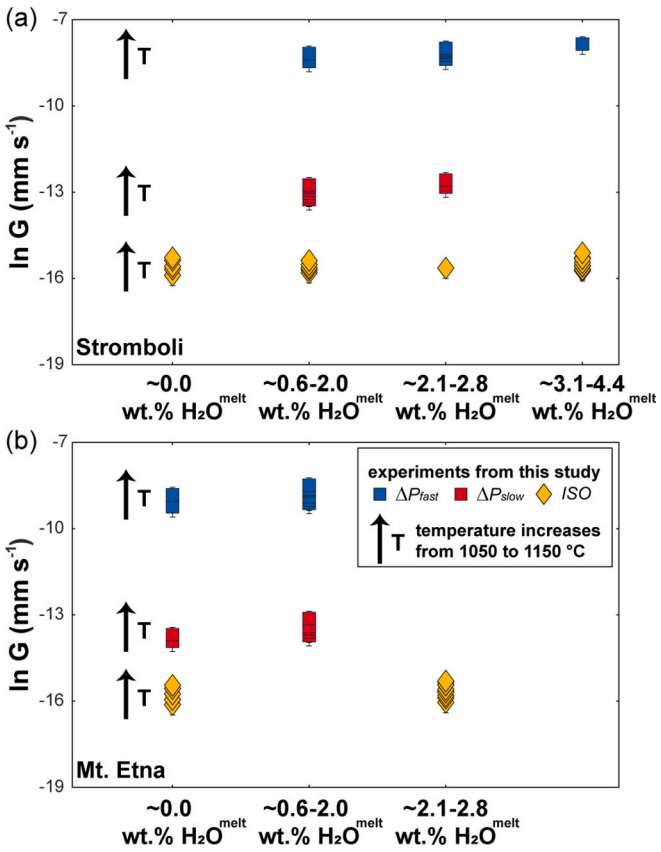

Fig. 1. Variation of plagioclase growth rate on a logarithmic scale as a function of isothermal-isobaric and fast-slow decompression conditions for Stromboli (a) and Etna (b) compositions.

temperature and melt-water content (Fig. 1a,b), in response to a faster chemical diffusion of crystal-forming components in the melt phase (Pupier et al., 2008; Shea and Hammer, 2013; Iezzi et al., 2014; Giuliani et al., 2020).

To understand the correlation between growth rate and other system variables in our experiments that may govern the crystallization process of plagioclase, we adopt multivariate regression analysis by selecting as input parameters the growth rate (ln$G$), degree of undercooling (ΔT as a proxy for the kinetic effect of decompression rate), crystallization temperature (T), crystallization time (ln$t$ as the sub-liquidus condition corresponding to the experimental duration), melt composition/structure (NBO/T^{melt}), and melt-water concentration (H_2O^{melt}). Undercooling and crystallization time parameters are expressed on a logarithmic scale to facilitate the mathematical treatment of their small and large quantities. Results from correlation matrix indicate that *p-values* for ln$t$ (0.00), ΔT (0.00), and T (0.04) are statistically significant for the overall description of ln$G$. Conversely, no obvious correlation is found between ln$G$ and H_2O^{melt} and NBO/T^{melt}, in accord with large *p-values* of 0.71 and 0.48, respectively. For subtle compositional ranges confined to mafic systems, the effects of melt-water content and melt depolymerization remain subordinate to the crystallization time and degree of undercooling. *Pearson's r* quantifies the strength of correlation between ln$G$ and ln$t$ (−0.99), ΔT (0.52), T (−0.25), H_2O^{melt} (−0.05), and NBO/T^{melt} (0.09). A strong negative dependence is determined between ln$G$ and ln$t$, whereas the correlation between ln$G$ and H_2O^{melt} and NBO/T^{melt} is very weak. The influence of ln$t$ on the magnitude of ln$G$ is markedly high and corresponds to 60%. Lower values are calculated for ΔT (21%) and T (12%). The influence of H_2O^{melt} and NBO/T^{melt} on ln$G$ is only 2% and 4%, respectively, and can be considered negligible.

3.3. Control of crystallization time on growth rate

The diagram ln*G* against ln*t* in Fig. 2a shows a net linear decay of plagioclase growth rate from this study with increasing crystallization time. This general trend reflects the achievement of chemical equilibrium over time by diffusive relaxation and minimization of supersaturation effects at the crystal-melt interface (Kirkpatrick, 1981; Kohut and Nielsen, 2004; Hammer, 2008; Pontesilli et al., 2019; Moschini et al., 2021). To understand the role played by relaxation kinetics on crystal growth, we must recall that at high supersaturation the crystal growth rate exceeds the diffusion of melt components, such that diffusive boundary layers enriched in incompatible components surround the crystal surfaces (Watson and Müller, 2009). Disequilibrium growth may take place in presence of a very thin and not detectable diffusive boundary layer around the crystal. This aspect is not trivial in mafic, depolymerized, low viscosity melts, where diffusion gradients are restricted to the interaction of cations at the crystal-melt interface over length scale from a few microns or even less (Watson and Müller, 2009). Under rapid growth conditions, plagioclase crystals develop elongate shapes and long sizes (i.e., high aspect ratios) to reduce latent heat and penetrate the diffusive boundary layer saturated by rate-limiting components for the crystal growth (i.e., Kirkpatrick and Kuo, 1981; Kohut and Nielsen, 2004). This corresponds to a morphological instability between plagioclase face and the diffusive boundary layer, such that plagioclase crystals grow in the direction of more relaxed melt regions. Conversely, at low supersaturation, the growth rate of plagioclase is slow and incompatible components in the melt are efficiently rejected away from the advancing crystal surface (Watson and Müller, 2009). As a result, the interface melt may easily supply chemical nutrients compatible with the lattice site of plagioclase crystals that develop planar faces and short sizes (i.e., low aspect ratios; Kirkpatrick and Kuo, 1981; Kohut and Nielsen, 2004).

Following the same approach of Moschini et al. (2021), a weighted least square regression analysis is performed on data plotted in Fig. 2a, by giving to each ln*G* value the proper amount of influence over the estimate that corresponds to a weight of 30% according to segmentation process and error propagation analysis. Logarithmic data are susceptible to uncertainties associated with the linearization of the model (i.e., heteroskedasticity; Hair et al., 1995). Therefore, error minimization by incorporating weights into the fitting criterion is extremely important to downweight outliers and reduce their impact on the regression model. Growth rate calculations may also suffer from lack of accurate knowledge concerning the crystallization time. Measuring the time lag caused by delayed crystal appearance due to early supersaturation effects is not a trivial task. The same issue is encountered in determining the exact time at which the crystal growth ceases, and chemical equilibrium is established at the crystal-melt interface. Bearing in mind these limitations, potentially aberrant data are filtered and not used for regression

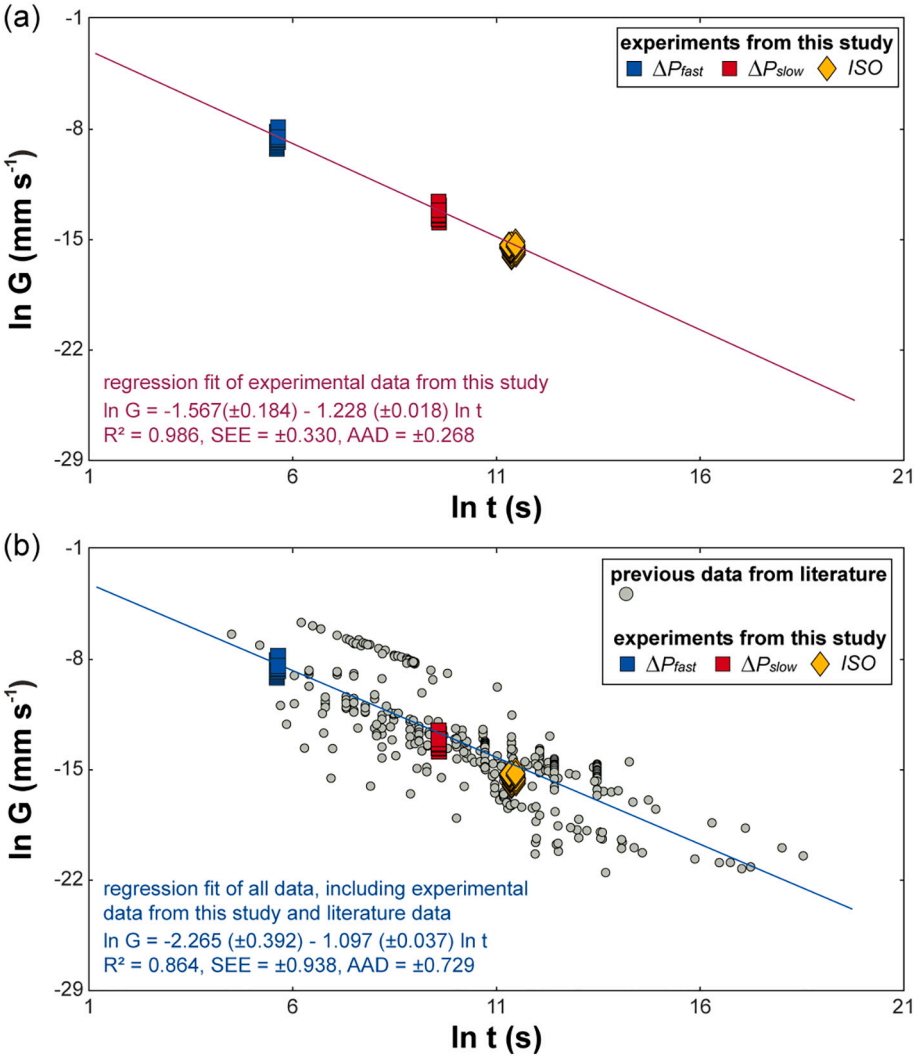

Fig. 2. Plot of growth rate from our experiments against time on a logarithmic scale (a). Comparison between growth rate from our experiments and those from literature reported in Supplementary Material 4 (b).

analysis. We cautiously consider as spurious ln$G$ values those returning estimates exceeding 95% confidence interval (2σ) of the model error. The algebraic form of the weighted least square linear regression equation is:

$$lnG = \beta_0 + \beta_1 lnt \quad (3)$$

The best regression constants solving Eq. (3) for our experiments are $\beta_0 = -1.567$ and $\beta_1 = -1.228$, with $R^2 = 0.986$, $SEE = \pm 0.330$, and $AAD = \pm 0.268$ (Fig. 2a).

By considering both plagioclase growth rates from this study and those from literature reported in Supplementary Material 4, we can also derive a global model with $\beta_0 = -2.265$ and $\beta_1 = -1.097$, with $R^2 = 0.864$, $SEE = \pm 0.938$, and $AAD = \pm 0.729$ (Fig. 2b). For this global data set, values of *Pearson's r* from multivariate regression analysis confirm that ln$G$ is prevalently controlled by ln$t$ (0.80) and subordinately by ΔT (0.15). Weak correlations are still found between ln$G$ and T (0.03), H_2O^{melt} (0.07), and NBO/T^{melt} (0.06). The magnitude of ln$G$ results primarily influenced by ln$t$ (72%) and secondarily by ΔT (13%). The influence related to T (3%), H_2O^{melt} (6%), and NBO/T^{melt} (5%) is minimal.

Model robustness and solidity are verified by perturbing Eq. (3) via Monte Carlo simulations over a normal distribution with the mean centered on ln$G$ and deviation close to *SEE* (Hair et al., 1995). After generating 1000 sets of hypothetical regression coefficients, probability density functions are used to analyze the Gaussian distribution of perturbed β_0 and β_1. For plagioclase growth rates from this study, the uncertainties of perturbed β_0 and β_1 are ± 0.184 and $\pm$ 0.018, respectively. For the global model, ~95% of perturbed β_0 and β_1 have uncertainties of ± 0.392 and $\pm$ 0.037, respectively. These quantities compare well with those derived by weighted least square regression analysis and their propagation in Eq. (3) produces perturbed model errors (ε) with mean values close to 25%.

3.4. Estimating eruptive timescales at Stromboli and Mt. Etna

Stromboli is a steady-state volcano whose eruptive activity is related to the dynamics of an open-conduit system undergoing continuous recharge, crystallization, and eruption (Francalanci et al., 2005, 2012; Ubide et al., 2019; Petrone et al., 2018, 2022). The normal eruptive activity at Stromboli consists of ejections of high-porphyritic (*Hp*) black scoria and lapilli during mild "Strombolian" explosions, which are interrupted by more violent explosions, major explosions and paroxysms, producing a characteristic low-porphyritic (*Lp*) light pumice (Métrich et al., 2010; Francalanci et al., 2012). Major explosions consist of single and/or multiple blasts with intervals of few seconds to minutes that do not affect the settled areas, whereas paroxysms refer to higher volumes of erupted juvenile material threatening the inhabitants and villages (Barberi et al., 1993). The Present-day activity (< 1.2 kyr) of Stromboli is fed by a vertically-extended mush column, which is periodically refilled with mafic magmas rising from the deeper *Lp*-reservoir ($P \approx$ 190–260 MPa, $T \geq 1150$ °C, and H_2O^{melt} up to ~3.8 wt%) and mixing with more differentiated magmas stored in the shallower *Hp*-reservoir ($P \approx$ 50–100 MPa, $T < 1150$, and H_2O^{melt} up to ~2.4 wt%) (Landi et al., 2004, 2006; Métrich et al., 2010; Di Stefano et al., 2020).

Most of plagioclase crystallization is related to extensive magma degassing within the uppermost segment of mush column. Syn-eruptive *Lp-Hp* magma mixing and mush cannibalism are also recorded by the marked chemical heterogeneities and complex textures of plagioclase phenocrysts, showing corroded cores, coarsely sieved mantles, overgrowth rims, and patchy to oscillatory zonations (Francalanci et al., 2005, 2012; Landi et al., 2004, 2006). In response to open-system crystallization conditions and mush remobilization phenomena, plagioclase corroded cores are in Sr isotopic disequilibrium with their host magmas (i.e., bulk rock analyses). Disequilibrium is caused by transport of antecrysts into shallower *Hp*-reservoirs by recurrent arrival of deeper *Lp*-magmas passing through the mush column (Francalanci et al., 2005, 2012; Landi et al., 2004, 2006).

With the purpose of modeling eruption timescales at Stromboli, we focus on scoria clasts from three paroxysms (05/04/2003, 15/03/2007, and 03/07/2019) and one major eruption (01/11/2017) that are characterized by abundant crystallization of plagioclase. A representative BSE photomicrograph of 05/04/2003 sample obtained at low magnification shows that scoria clasts are dominated by plagioclase (Supplementary Material 5). Zoom-in views highlight that plagioclase populations with $L > 0.3$ mm are characterized by strong disequilibrium features as described above, whereas plagioclase populations with $L \leq$ 0.3 mm are texturally homogeneous (Supplementary Material 5). This observation is in close agreement with the CSD study by Fornaciai et al. (2009) outlining that changes in slopes and intercepts derived for large plagioclase crystals are caused by cyclic dissolution/recrystallization processes during magma mixing dynamics. Conversely, steeper CSD gradients attained at smaller crystal sizes identify plagioclase crystals that do not show resorption features because of growth via *syn*-eruptive magma depressurization and degassing. Regression analysis of *N(L)* against L data for these small crystals returns values of m and N_0 varying from −16.08 to −17.45 and from 4.73 to 8.16, respectively (Supplementary Material 5). The timescale of crystal growth is quantified by taking into consideration the dynamic temporal evolution of G with t, as described in Eq. (3). Following Moschini et al. (2021), we substitute Eq. (3) into the slope $m = 1 / (G \times \tau)$ of CSD Eq. (1) and then rearrange the algebraic expression to isolate the crystallization time of plagioclase as:

$$G = t^{\beta_1}\, exp\beta_0, \quad (4)$$

$$m = -\frac{1}{\left[t_{max}^{(\beta_1+1)}\, exp\beta_0\right]} \quad (5)$$

and

$$t = \left(-\frac{1}{m\, exp\beta_0}\right)^{\left(\frac{1}{\beta_1+1}\right)} \quad (6)$$

Using regression coefficients from Eq. (3) from our experiments, we estimate crystallization times of ~5 ± 1 (05/04/2003), ~4 ± 1 (15/07/2007), ~5 ± 1 (01/11/2017), and ~ 3 ± 1 (03/07/2019) min. For the sake of completeness, we also test regression coefficients for the global model, which yields comparable crystallization times of ~8 ± 2 (05/04/2003), ~5 ± 1 (15/07/2007), ~7 ± 2 (01/11/2017), and ~ 3 ± 1 (03/07/2019) min. Irrespective of the equation used, we stress that estimates in the order of minutes corroborates data from numerical simulations on *syn*-eruptive disequilibrium plagioclase crystallization in basaltic magma ascent dynamics at Stromboli, Mt. Etna, and Kilauea volcanos (La Spina et al., 2016). Results from one-dimensional multiphase multicomponent steady-state modeling indicate that, after magma depressurization, equilibrium plagioclase content is achieved in ~100 min. However, fast disequilibrium ascent of magma within the conduit causes rapid growth of plagioclase microlites over a timescale of 2 min when the gas exsolution timescale is <3 min (La Spina et al., 2016). In situ four-dimension (4D) (3D plus time) kinetic crystallization experiments using fast synchrotron X-ray microtomography provide evidence that undercooling drives exceptionally rapid (in minutes) microlite crystallization during rapid magma ascent in highly explosive basaltic eruptions (Arzilli et al., 2019). Skeletal plagioclase crystallization are observed to develop at ΔT between 60 and 140 °C with a growth rate in the order of 1–4 mm h^{-1} (Supplementary Table 2 in Arzilli et al., 2019). These large degrees of undercooling are produced by the adiabatic expansion of exsolved volatiles and mitigated by the latent heat of crystallization during syn-eruptive magma ascent (Arzilli et al., 2019). Considering that strong degassing-induced crystallization at Stromboli is expected to take place in the last 2 km of the conduit (cf. Di Stefano et al., 2020), we calculate magma ascent rates of ~7–10 m s^{-1} (regression of mafic data set) and ~ 4–10 m s^{-1} (regression of overall

data set) for paroxysmal and major eruptions, in agreement with previous estimates for mafic alkaline magmas at Stromboli, Mt. Etna, and Kilauea (~1–23 m s^{-1}; La Spina et al., 2016, 2021; Polacci et al., 2019; Moschini et al., 2021) or more silicic explosive eruptions worldwide (~0.5–50 m s^{-1}; Cassidy et al., 2018).

As a further application of growth rate data from this study, we also consider large plagioclase phenocrysts ($L > 0.5$ mm) from lava flows at Mt. Etna, the largest sub-aerial volcano in Europe and one of the most active on Earth (Armienti et al., 1994, 1997). Over the last 300 kyr, Mt. Etna produced abundant trachybasalt to basaltic trachyandesite and trachyandesite lavas, mainly characterized by the ubiquitous occurrence of clinopyroxene, plagioclase and titanomagnetite (Mollo et al., 2015a). The plumbing system has a multifaceted geometry, variable in space and time, and consisting of storage zones at different depths, where primitive magmas undergo fractional crystallization, degassing, and mixing processes (Armienti et al., 2013). An open-conduit system is persistently filled with magma feeding spectacular explosive Strombolian eruptions and lava fountains from the summit craters. Effusive flank eruptions occur as both lateral eruptions draining magma from the central conduit (Corsaro et al., 2009) and as eccentric (peripheral) eruptions bypassing the central conduit and draining magma from the deeper feeding system (Andronico et al., 2005). Petrological studies outline that intratelluric crystals generally equilibrate at $P \approx$ 100–500 MPa, $T \approx$ 1000–1200 °C, and $H_2O^{melt} \approx$ 1–3 wt% (Métrich et al., 2004; Armienti et al., 2013; Mollo et al., 2015a, 2018).

Armienti et al. (1994) reports CSD data for plagioclase phenocrysts from lava flows outpoured over an eruptive period started on December 1991 and ended in March 1993. The eruption started from of a fissure near the South East Crater and produced ~300 × 10^6 m^3 of material. Plagioclase dominates the paragenesis of all porphyritic rock samples. In CSD plots, larger phenocrysts with euhedral, tabular shapes are distributed along nearly horizontal trends, identifying a population of intratelluric crystals in equilibrium under deep-seated conditions (i.e., 570–750 MPa and 1140–1160 °C; Armienti et al., 1994). Importantly, isotopic and geochemical data demonstrate that large-scale magma mixing never occurred and that 1991–1993 eruptions represents a single magma batch (Armienti et al., 1994). A similar conclusion is also reported in a companion study by Armienti et al. (1997), in which textural analysis of plagioclase is extended to the eccentric 1974 lava flow and other lavas containing centimeter-sized plagioclase phenocrysts from 1614, 1624, and 1723 subterminal and flank eruptions. By interpolating slopes (from −14 to −17 mm^{-1}) of CSD curves from Armienti et al. (1994, 1997) and plagioclase growth rates from isothermal-isobaric experiments (~10^{-7} mm s^{-1}), we obtain crystal residence times from 3 (±0.25) to 9 (±2.25) years, in accord with low degrees of undercooling (<30 °C; Orlando et al., 2008) and slow cooling rates (0.16 °C h^{-1}; Cashman, 1993) in the lowermost parts of the plumbing system, where most of the volatiles are retained into the melt and/or exsolve gradually during slow degassing (Armienti et al., 2013).

4. Plagioclase and melt compositional changes

4.1. Plagioclase cation substitutions and exchange partition coefficients

In our experiments, plagioclase saturation temperatures range from 1050 °C when H_2O^{melt} = 4.4 wt% to 1150 °C when H_2O^{melt} = 0 wt% (Supplementary Material 1). The compositional variation of plagioclase is displayed in Fig. 3 as a function of T and H_2O^{melt}. Appreciable linear correlations (R^2 = 0.51–0.67) are measured between plagioclase cation fractions and the experimental temperature, with fast and slow decompression data that overlap to compositions obtained isothermally at 1050 and 1100 °C. X^{pl}_{Ca} and X^{pl}_{Mg} are preferential incorporated in plagioclase with increasing T, whereas values of X^{pl}_{Na} and X^{pl}_{Fe} decrease (Fig. 3). Regression fits depicted by X^{pl}_{Ca} and X^{pl}_{Na} show opposite directions with almost identical R^2 = 0.63–0.64, as a proxy for the well-established heterovalent coupled substitution [$^{M}Na^{+}$, $^{T}Si^{4+}$] ↔ [$^{M}Ca^{2+}$, $^{T}Al^{3+}$] (Smith and Brown, 1988; Housh and Luhr, 1991). In contrast to the apparent control of T on cation incorporation, the

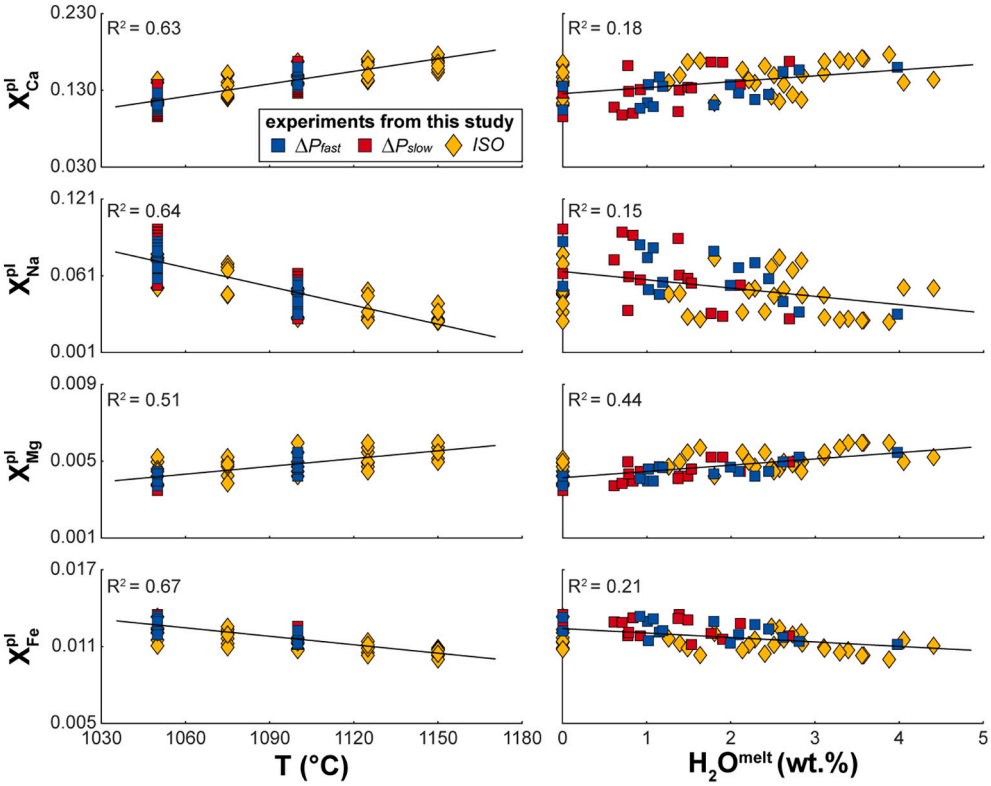

Fig. 3. Compositional variation of plagioclase crystals from isothermal-isobaric and fast-slow decompression conditions as a function of temperature and melt-water content.

strength of correlation between plagioclase cation fractions and H_2O^{melt} is generally weak for X^{pl}_{Ca}, X^{pl}_{Na}, and X^{pl}_{Fe} ($R^2 = 0.15$–0.21), with a slightly better fit for X^{pl}_{Mg} ($R^2 = 0.44$) (Fig. 3).

The site occupancies of Fe and Mg are particularly difficult to establish for plagioclase because these cations show heterovalent substitution (e.g., Fe^{2+} and Fe^{3+}) and/or site splitting (e.g., Mg^{2+} and Fe^{2+}) (Lindsley and Smith, 1971; Smith and Brown, 1988; Sugawara, 2001; Xue and Morse, 1994). Fe^{3+} substitutes for Al^{3+} in tetrahedral coordination as $Ca(Fe^{3+},Al^{3+})Si_2O_8$, whereas Fe^{2+} and Mg^{2+} can alternatively enter both the M- and T-sites to form $(Fe^{2+},Mg^{2+})Al_2Si_2O_8$ and $Ca(Fe^{2+},Mg^{2+})Si_3O_8$ components, respectively (Smith, 1974; Longhi et al., 1976; James and McGee, 1992; Peters et al., 1995; Sugawara, 2001). However, no more than about 10% of Fe^{2+} and Mg^{2+} substitutes in the form of $(Fe,Mg)Al_2Si_2O_8$ and both cations can be reasonably assumed as tetrahedrally coordinated (Sugawara, 2001 and references therein). Substitution mechanisms of these cations in plagioclase are strictly controlled by the compositional dependence of crystal-melt equilibrium reactions on the activities of melt components (Longhi et al., 1976; Peters et al., 1995). According to Longhi et al. (1976), we can consider only the ideal term of these reactions by plotting mol.% of MgO and FeO (i.e., total iron as FeO from microprobe analysis) in plagioclase against those of melt oxides. The geochemical evolution of MgO and FeO in plagioclase scales with the magnitude of melt oxides (Fig. 4a), with plagioclase crystals from mafic alkaline experiments typically enriched in total iron as a result of high oxidizing equilibration conditions (see Mollo et al., 2011 for further details). Regression fits indicate that experimental partition coefficients (K) of MgO and FeO ($K_{Mg} = 0.04$ and $K_{Fe} = 0.07$) are almost identical to those determined by Longhi et al. (1976) for terrestrial basalts ($K_{Mg} = 0.04$ and $K_{Fe} = 0.06$).

Wilke and Behrens (1999) show that K_{Fe} measured between plagioclase and low-T (750–850 °C) silicic melts (SiO_2 = 62–68 wt% and FeO_{tot} = 0.6–1.4 wt%) increases with increasing temperature. However, as explained by Wilke and Behrens (1999), K_{Fe} is strongly controlled by the oxygen fugacity imposed to the experimental charge, thus overwhelming the effects of temperature and melt components on iron incorporation reactions. This implies that K_{Fe} is independent of temperature when most of FeO_{tot} consists of ferric iron under reducing crystallization conditions (Sato, 1989; Phinney, 1992; Aigner-Torres et al., 2007). For example, little or no variations are observed for K_{Fe} calculated by Aigner-Torres et al. (2007) at high-T (1180–1220 °C) and low-fO_2 (IW-QFM buffer) for basaltic melts (SiO_2 = 49–52 wt% and FeO_{tot} = 8–10 wt%). Conversely, the authors document that changing iron speciation from Fe^{2+} to Fe^{3+} in oxidized melts causes K_{Fe} to decrease with increasing T (Aigner-Torres et al., 2007), as described by the negative X_{Fe}-T trend derived for mafic alkaline melts (Fig. 3). Owing to the relative high oxidation conditions of our experiments and natural alkaline magmas at Stromboli and Mt. Etna ($fO_2 \geq$ NNO + 1.5; e.g., Mollo et al., 2015a), most of the total iron in the melt is ferrous iron (i.e., Fe_2O_3 > 60%), as calculated by the model of Kress and Carmichael (1991). Analogously, the partitioning equations of Sugawara (2001) indicate that Fe_2O_3 accounts for ~66–78% of total iron in plagioclase. We can therefore reappraise the plagioclase-melt compositional variation displayed in Fig. 4a by considering iron speciation and using equilibrium reactions for $CaMgSi_3O_8$ and $CaFeAlSi_2O_8$ components of the same type as those reported in Peters et al. (1995):

$$CaO^{melt} + MgO^{melt} + 3SiO_2{}^{melt} = CaMgSi_3O_8{}^{pl} \quad (7)$$

$$K_{eq} = \left[CaMgSi_3O_8{}^{pl}\right] \Big/ \left[CaO^{melt}\ MgO^{melt}\ \left(SiO_2{}^{melt}\right)^3\right] \quad (8)$$

$$K_{Mg} = \left[MgO^{pl}\right] \Big/ \left[MgO^{melt}\right] \propto K_{eq} \left[CaO^{melt}\ \left(SiO_2{}^{melt}\right)^3\right] \quad (9)$$

$$CaO^{melt} + 0.5Fe_2O_3{}^{melt} + 0.5Al_2O_3{}^{melt} + 2SiO_2{}^{melt} = CaFeAlSi_2O_8{}^{pl} \quad (10)$$

$$K_{eq} = \left[CaFeAlSi_3O_8{}^{pl}\right] \Big/ \left[CaO^{melt}\ \left(Fe_2O_3{}^{melt}\right)^{0.5}\ \left(Al_2O_3{}^{melt}\right)^{0.5}\ \left(SiO_2{}^{melt}\right)^2\right] \quad (11)$$

$$K_{Fe} = \left[Fe_2O_3{}^{pl}\right] \Big/ \left[Fe_2O_3{}^{melt}\right] \propto K_{eq} \left[CaO^{melt}\ \left(Al_2O_3{}^{melt}\right)^{0.5}\ \left(SiO_2{}^{melt}\right)^2\right] \quad (12)$$

To solve Eq. (9) and Eq. (12), the activity of melt components is calculated with the two-lattice melt model of Nielsen and Drake (1979) where the melt is assumed as two-independent quasi-lattices formed by network-former and network-modifier cations. These hypothetical thermodynamic components are assumed as proxies for the actual melt species as indicated by the positive linear variation of K^{pl}_{Mg} and K^{pl}_{Fe} as a function of melt oxide activities (Fig. 4b), in accord with the dominant effect of melt energetics on cation occupancies in plagioclase T-site (Peters et al., 1995).

As already reported by several authors (Longhi et al., 1976; Aigner-Torres et al., 2007; Mollo et al., 2011), there is no dependence of Fe—Mg exchange partition coefficient [$Kd^{pl-melt}_{Fe-Mg} = (X^{pl}_{Fe}/X^{pl}_{Mg})/(X^{melt}_{Fe}/X^{melt}_{Mg})$] on T and H_2O^{melt} ($R^2 = 0.01$–0.31), showing an almost constant value of 2.1

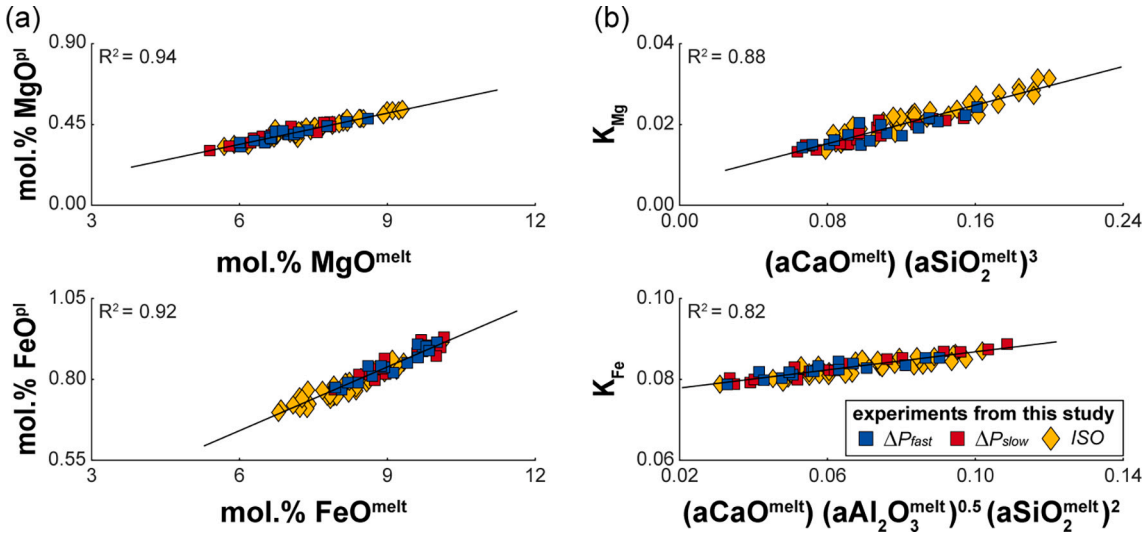

Fig. 4. Plot of mol.% of MgO and FeO (i.e., total iron as FeO from microprobe analysis) in plagioclase against those of melt oxides from isothermal-isobaric and fast-slow decompression conditions (a). Plot of plagioclase-melt partition coefficients for iron and magnesium against melt components calculated with the two-lattice melt model of Nielsen and Drake (1979) (b).

± 0.4 (Fig. 5). This result closely matches with the range of 2.2 ± 0.1 calculated by Mollo et al. (2011) for crystals formed from a trachybasalt equilibrated under anhydrous conditions at P = 500 MPa, T = 1000–1100 °C and fO_2 = NNO + 1.5. The authors performed also cooling rate experiments inducing rapid plagioclase growth and formation of dendritic crystals surrounded by a diffusive melt with thickness of ~50 μm. Because of strong deviations from chemical equilibrium, $K_{Fe-Mg}^{pl-melt}$ is measured to decrease by Mollo et al. (2011) towards a disequilibrium value of 1.6 ± 0.1. Fe and Mg are incompatible with the lattice site of plagioclase and their partitioning behaviors are extremely sensitive to cation incorporation at non-equilibrium proportions during dendritic crystal growth via diffusion-controlled kinetics (Mollo et al., 2011). The lack of both dendrites and thick diffusive boundary layers in decompression experiments from this study and the constancy of $K_{Fe-Mg}^{pl-melt}$ suggest attainment of local chemical equilibrium at the interface between the advancing plagioclase surface and surrounding melt (Di Fiore et al., 2021; Lang et al., 2021). The entry of cations in plagioclase lattice site at near-equilibrium partitioning conditions is mainly due to the low viscosity of mafic melts and the enhancing effect of water on cation mobility not only under static conditions but also during decompression-driven crystallization. During disequilibrium degassing, water transfer from the melt into vapor phase is less efficient than equilibrium volatile fractionation (Bai et al., 2008). Because dissolved water is partly retained in the supersaturated melt, the transfer rate of cations at the crystal-melt interface is enhanced and the length scale of diffusion fields around decompressed acicular crystals cannot be resolved with microprobe analysis (e.g., Mollo et al., 2018).

Fig. 5 shows that the An-Ab (or Ca—Na) exchange partition coefficient ($K_{An-Ab}^{pl-melt}$ or $K_{Ca-Na}^{pl-melt}$) is strictly dependent on T ($R^2 = 0.73$) and there is no statistically significant correlation between $K_{An-Ab}^{pl-melt}$ and H_2O^{melt}, at least for the subset of data investigated in this study and specific to mafic alkaline magmas. This lack of correlation is apparently in contrast with the well-established increase of $K_{An-Ab}^{pl-melt}$ with increasing the amount of water dissolved in calc-alkaline melts proposed by Sisson and Grove (1993). For experimental plagioclase-melt pairs obtained by equilibrating calc-alkaline basalts to rhyolites under water-saturated conditions ($P \approx$ 100–500 MPa and $T \approx$ 940–1120 °C), Sisson and Grove (1993) found a progressive increase of $K_{An-Ab}^{pl-melt}$ from ~1.7 for $H_2O^{melt} \approx$ 2 wt%, ~3–4 for $H_2O^{melt} \approx$ 4 wt%, and ~ 5.5 for $H_2O^{melt} \approx$ 6 wt%. These values were obtained by regressing experimental data in the diagram An^{melt}/Ab^{melt} against An^{pl}/Ab^{pl} and forcing the fit to pass through the origin of axis. Here we extend the data set used by Sisson and Grove (1993) to calc-alkaline compositions from Lange et al. (2009) and Waters and Lange (2015) obtained under both hydrous and anhydrous conditions ($P \approx$ 0.1–500 MPa, $T \approx$ 800–1235 °C, and $H_2O^{melt} \approx$ 0–8 wt%) and then compare them with mafic alkaline experiments. In Fig. 6, data are grouped as calc-alkaline basalts-andesites ($T \approx$ 1100–1235 °C and $H_2O^{melt} \approx$ 0–2 wt%), calc-alkaline dacites-rhyolites ($T \approx$ 800–1060 °C and $H_2O^{melt} \approx$ 2–8 wt%), and mafic alkaline melts ($T \approx$ 1050–1150 °C and $H_2O^{melt} \approx$ 0.0–4.4 wt%), returning $K_{An-Ab}^{pl-melt}$ of 0.8–2.1, 2.5–7.5, and 1.6–3.5, respectively. Importantly, high-T, low-H_2O^{melt} calc-alkaline basalts-andesites correspond to low $K_{An-Ab}^{pl-melt}$ endmembers, whereas low-T, high-H_2O^{melt} calc-alkaline dacites-rhyolites refer to high $K_{An-Ab}^{pl-melt}$ endmembers (Fig. 6). Because of interrelation between T and H_2O^{melt}, the diagram An^{melt}/Ab^{melt} against An^{pl}/Ab^{pl} cannot unequivocally discriminate and isolate the effect of temperature from that of dissolved water. While the solubility of water in the melt increases with increasing its silicic character, the onset of plagioclase crystallization takes place at lower temperatures as both liquidus and solidus curves of the binary loop for the Ab-An system are depressed by water addition. As a consequence, $K_{An-Ab}^{pl-melt}$ values obtained for mafic alkaline melts at intermediate T and H_2O^{melt} are bounded between those derived for high-T, low-H_2O^{melt} and low-T, high-H_2O^{melt} calc-alkaline compositions.

In terms of An-Ab components, our experimental plagioclase crystals show $An_{47–87}$ and $Ab_{12–48}$ compositions (expressed in percentage). As for X_{Ca}^{pl} and X_{Na}^{pl} trends depicted in Fig. 3, $An_{47–87}$ and $Ab_{12–48}$ compositions are more tightly correlated with T ($^{An}R^2 = 0.65$ and $^{Ab}R^2 = 0.64$) rather than H_2O^{melt} ($^{An}R^2 = 0.15$ and $^{Ab}R^2 = 0.14$). Experimental crystals also reproduce most of natural plagioclase phenocrysts at Mt. Etna ($An_{43–88}$ and $Ab_{10–48}$) and Stromboli ($An_{41–90}$ and $Ab_{8–50}$), as reported in the GEOROC database (http://georoc.mpch-mainz.gwdg.de).

4.2. Tracking differentiation conditions of natural mafic alkaline melts

Residual glass compositions from our experiments are comparatively plotted in Fig. 7 against *Hp-Lp*-glasses and 2003–2020 bulk rocks from Stromboli, as well as historic (from 15 kyr to 1886) and recent (2001−2021) bulk rocks from Mt. Etna (data from the GEOROC database). Experimental glasses become more differentiated as the degree of crystallization increases with decreasing T and H_2O^{melt}. Both slow and fast decompression experiments are also characterized by water exsolution and consequent formation of more silicic- and alkali-rich melts (Fig. 7).

For Stromboli, mafic bulk rocks and *Lp*-glasses are described by experiments carried out at $T \geq$ 1100 °C and $H_2O^{melt} \geq$ 1.5 wt% (Fig. 7). These compositions are classified as high-K and shoshonitic basalts (Francalanci et al., 2013) and match with primitive, undegassed *Lp*-magmas stored at $P \approx$ 200–300 MPa (~7–10 km depth for an average

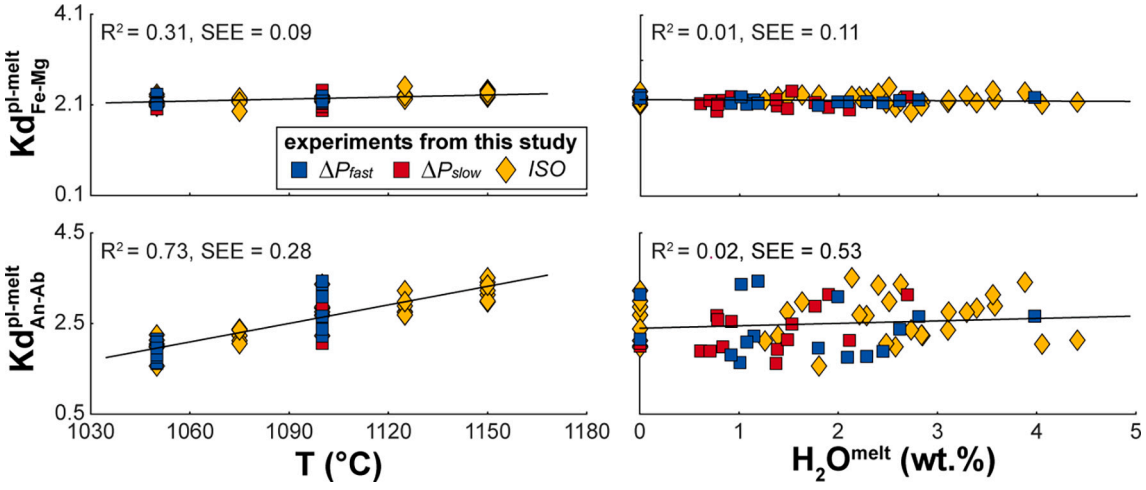

Fig. 5. Variation of Fe—Mg and An-Ab exchange partition coefficients between plagioclase and melt as a function of temperature and melt-water concentration. Data from isothermal-isobaric and fast-slow decompression experiments.

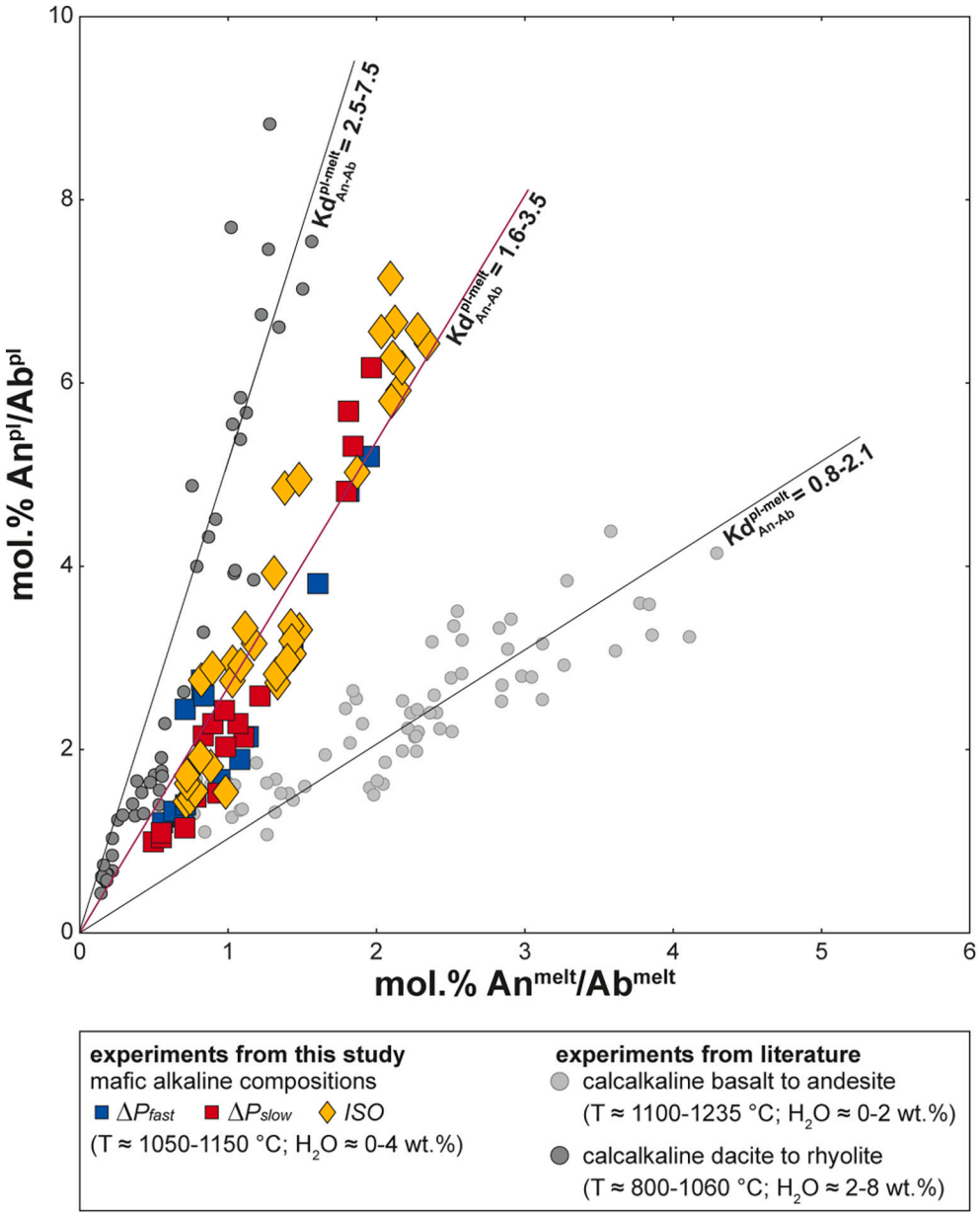

Fig. 6. Plot of An^{melt}/Ab^{melt} against An^{pl}/Ab^{pl} for isothermal-isobaric and fast-slow decompression experiments carried out on mafic alkaline compositions from this study, compared with literature data from Sisson and Grove (1993), Lange et al. (2009), and Waters and Lange (2015). Data are grouped as calc-alkaline basalts-andesites ($T \approx$ 1100–1235 °C and $H_2O^{melt} \approx$ 0–2 wt%), calc-alkaline dacites-rhyolites ($T \approx$ 800–1060 °C and $H_2O^{melt} \approx$ 2–8 wt%), and mafic alkaline melts ($T \approx$ 1050–1150 °C and $H_2O^{melt} \approx$ 0.0–4.4 wt%).

crustal density of 2700 kg m^{-3}; Allard et al., 2000), $T \approx$ 1165–1175 °C, and $H_2O^{melt} \approx$ 2.0–3.5 wt% (Clocchiatti, 1981; Métrich et al., 2010; Di Stefano et al., 2020). More evolved *Hp*-glasses and bulk rocks with shoshonitic compositions are experimentally reproduced at $T \leq$ 1100 °C and $H_2O^{melt} <$ 1.5 wt% (Fig. 7). These conditions correspond to a low-*P* storage region at 50–100 MPa (~2–4 km depth) where *Hp*-magmas undergo strong cooling and degassing phenomena (Métrich et al., 2010; Francalanci et al., 2013; Di Stefano et al., 2020).

For Mt. Etna, experimental glasses synthetized at $T \geq$ 1100 °C and $H_2O^{melt} =$ 2.1–6.3 wt% agree with geochemical modeling and melt inclusions characterization of 2001–2021 trachybasaltic eruptions (Fig. 7), which are fed by recurring inputs of fresh magmas stored at $P \geq$ 100 MPa (Métrich and Rutherford, 1998; Métrich et al., 2004; Armienti et al., 2013; Giacomoni et al., 2018; Mollo et al., 2015b, 2018). Note that the plumbing system at Mt. Etna undergoes little crystallization at depth, as most of its water concentration is retained in the melt by lowering its liquidus temperature and the degree of crystallization (Perinelli et al., 2016). On the other hand, historic eruptions with basaltic trachyandesite compositions are obtained at $T <$ 1100 °C and $H_2O^{melt} =$ 0.0–2.8 wt% (Fig. 7). These differentiated magmas originate by degassing-induced crystallization at very shallow depths ($P <$ 100 MPa), when the degree of crystallization is higher than 20–25% owing to the enlargement of plagioclase stability field (Vetere et al., 2015). Low-*T*, low-H_2O^{melt} isothermal-isobaric experiments and slow-fast decompression experiments describe quite well this mechanism, thereby returning plagioclase-dominated phase assemblages with crystal contents variable from ~30 to ~40%.

5. Thermodynamic and statistical modeling of plagioclase-melt equilibrium

5.1. Preliminary considerations

For the simplest formula of An in plagioclase, the fusion reaction can be expressed as:

$$CaAl_2Si_2O_8{}^{pl} = CaAl_2Si_2O_8{}^{melt} \quad (13)$$

At the equilibrium, the chemical potential μ_{An} is the same in both

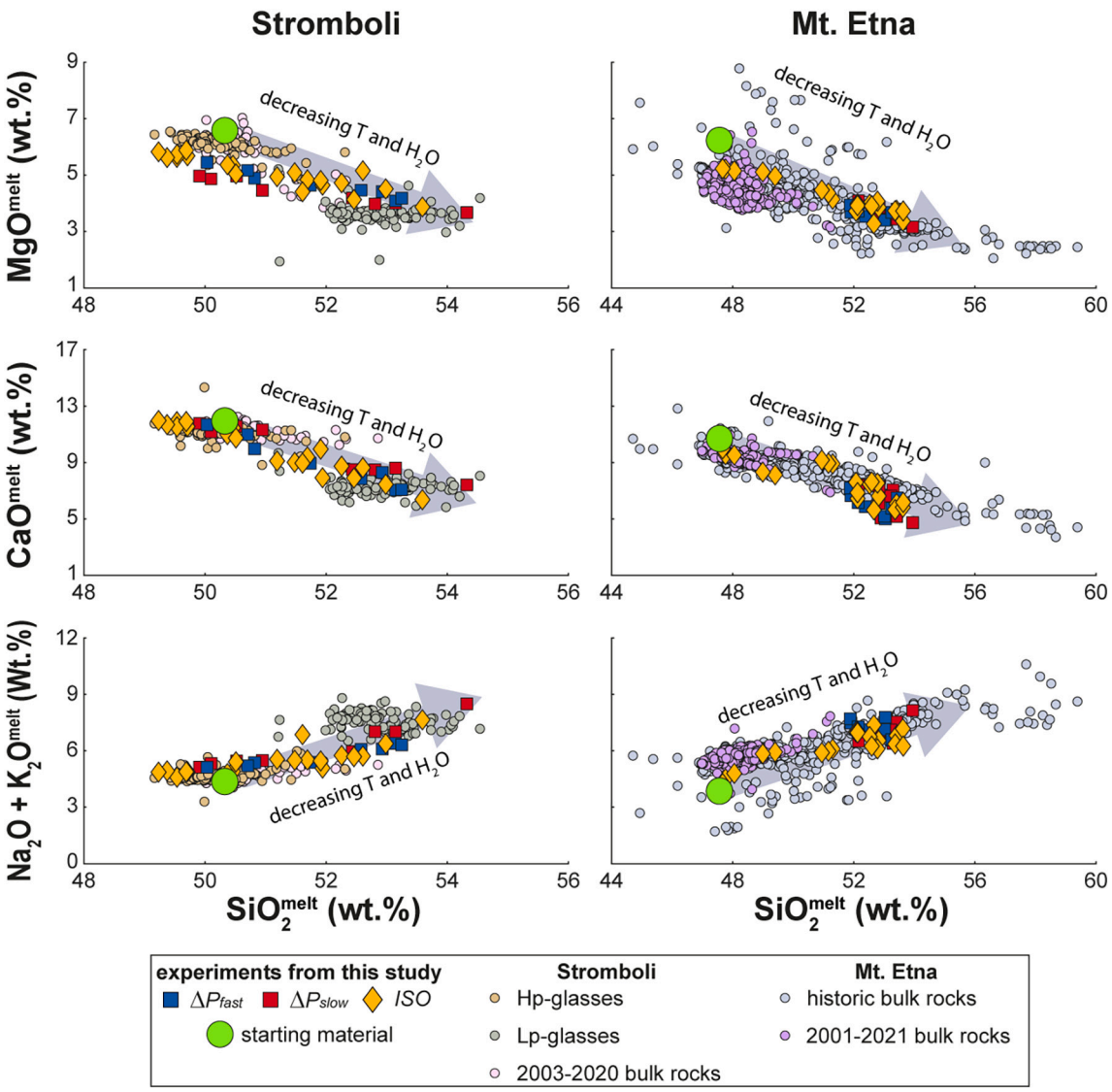

Fig. 7. Compositional variation of melt major oxides from isothermal-isobaric and fast-slow decompression experiments is compared with natural bulk rock compositions of magmas erupted at Stromboli and Mt. Etna.

plagioclase and melt:

$$\mu_{\mathrm{An}}^{pl} = \mu_{\mathrm{An}}^{melt} \tag{14}$$

$$\mu_{\mathrm{An}}^{pl} = \mu_{\mathrm{An}}^{o\ pl} + RTln\left(a_{\mathrm{An}}^{pl}\right) \tag{15}$$

$$\mu_{\mathrm{An}}^{melt} = \mu_{\mathrm{An}}^{o\ melt} + RTln\left(a_{\mathrm{An}}^{melt}\right) \tag{16}$$

$$\mu_{\mathrm{An}}^{o\ pl} + RTln\left(a_{\mathrm{An}}^{pl}\right) = \mu_{\mathrm{An}}^{o\ melt} + RTln\left(a_{\mathrm{An}}^{melt}\right) \tag{17}$$

$$\mu_{\mathrm{An}}^{pl} - \mu_{\mathrm{An}}^{melt} = \Delta\mu_{An} = 0 = \Delta G_{An}^{0}(P,T) + RTln\left(\frac{a_{\mathrm{An}}^{melt}}{a_{\mathrm{An}}^{pl}}\right) \tag{18}$$

For a standard-state of pure An at the pressure and temperature of interest, $\Delta G_{An}^{o}(P,T)$ is referred to as the standard Gibbs free energy of reaction (Glazner, 1984; Lange et al., 2009; Waters and Lange, 2015; Namur et al., 2012; Putirka, 2017). $\Delta G_{An}^{o}(P,T)$ is expressed in kJ mol^{-1} and changes as a function of both pressure (P in GPa) and absolute temperature (T in K) but is independent of plagioclase and melt compositions. The activity term a_{An} corresponds to the product of the molar fraction X_{An} and activity coefficient γ_{An}. For an ideal solution model, $\gamma_{\mathrm{An}} = 1$ and $a_{\mathrm{An}} = X_{\mathrm{An}}$. R is the gas constant in J K^{-1} mol^{-1}. Considering the equilibrium constant K_{An}^{eq} of the fusion reaction of An, Eq. (18) can be rewritten as:

$$\frac{\Delta G_{An}^{o}(P,T)}{RT} = ln\left(K_{\mathrm{An}}^{eq}\right) = ln\left(a_{\mathrm{An}}^{pl}\right) - ln\left(a_{\mathrm{An}}^{melt}\right) \tag{19}$$

The Gibbs free energy change from Eq. (19) has the thermodynamic form:

$$\Delta G_{An}^{o}(P,T) = \Delta H_{An}^{o}(T) - T\Delta S_{An}^{o}(T) + \int_{1}^{P} \Delta V_{T\ An}^{o}(P)dP \tag{20}$$

where $\Delta H_{An}^{o}(T)$ and $\Delta S_{An}^{o}(T)$ are the standard state change in molar enthalpy and entropy, respectively, for the pure An in plagioclase and melt phases. $\Delta V_{T\ An}^{o}(P)$ is the change in molar volume as a function of pressure (Glazner, 1984; Lange et al., 2009; Waters and Lange, 2015; Namur et al., 2012; Putirka, 2017). This thermodynamic quantity is calculated at the temperature of An reaction by assuming an initial pressure of 1 bar (= 0.0001 GPa).

Along the melting curve of pure An, the equilibrium constant K_{An}^{eq} of Eq. (13) is close to 1 as both plagioclase and melt phases are pure. $\Delta G_{An}^{fusion}(T_m) = \Delta H_{An}^{fusion}(T_m) - T\Delta S_{An}^{fusion}(T_m) = 0$ and $\Delta S_{An}^{fusion}(T_m) = [\Delta H_{An}^{fusion}(T_m)]/T_m$ at the melting temperature T_m of 1 bar pure phases.

The thermodynamic quantities governing the fusion reaction of An at the *P-T* of interest are reappraised as:

$$\Delta G^{fusion}_{An}(P,T) = \Delta H^{fusion}_{An}(T) + \Delta S^{fusion}_{An}(T) + \Delta V^{fusion}_{T\ An}(P) \quad (21)$$

$$\Delta H^{fusion}_{An}(T) = \left[\Delta H^{fusion}_{An}(T_m) + \int_{Tm}^{T} \Delta C_{p\ An} dT\right] \quad (22)$$

$$\Delta S^{fusion}_{An}(T) = \left[\frac{\Delta H^{fusion}_{An}(T_m)}{T_m} + \int_{Tm}^{T}\left(\frac{\Delta C_{p\ An}}{T}\right) dT\right] \quad (23)$$

$$\Delta V^{fusion}_{T\ An}(P) = V^{melt}_{T\ An}(P) - V^{pl}_{T\ An}(P) \quad (24)$$

where $\Delta C_{p\ An}$ is the difference in isobaric heat capacity between plagioclase and melt. $C^{melt}_{p\ An}$ is assumed to be constant over the temperature range of interest, whereas $C^{pl}_{p\ An}$ is approximated to a polynomial function of *T*, in agreement with Glazner (1984).

The same considerations reported above can be extended to pure Ab component and the An-Ab exchange reaction between plagioclase and melt:

$$CaAl_2Si_2O_8{}^{pl} + NaAlSi_3O_8{}^{melt} = CaAl_2Si_2O_8{}^{melt} + NaAlSi_3O_8{}^{pl} \quad (25)$$

Eq. (19) can be rewritten as:

$$\frac{\Delta G^{o}_{An}(P,T) - \Delta G^{o}_{Ab}(P,T)}{RT} = \frac{\Delta G^{o}_{An-Ab}(P,T)}{RT} = ln(K^{eq}_{An-Ab}) = ln\left(\frac{a^{pl}_{An}}{a^{pl}_{Ab}}\right) - ln\left(\frac{a^{melt}_{An}}{a^{melt}_{Ab}}\right) \quad (26)$$

The difference between the Gibbs free energies of plagioclase and melt components in equilibrium at the same *P-T* conditions is:

$$\Delta G^{o}_{An-Ab}(P,T) = \Delta H^{o}_{An-Ab}(T) - T\Delta S^{o}_{An-Ab}(T) + \int_{1}^{P} \Delta V^{o}_{T\ An-Ab}(P) dP = \left[\Delta H^{o}_{An-Ab}(T_m) + \int_{Tm}^{T} \Delta C_{p\ An-Ab} dT\right] - T\left[\frac{\Delta H^{o}_{An-Ab}(T_m)}{Tm} + \int_{Tm}^{T}\left(\frac{\Delta C_{p\ An-Ab}}{T}\right) dT\right] + \int_{1}^{P} \Delta V^{o}_{T\ An-Ab}(P) dP \quad (27)$$

where $\Delta H^{o}_{An-Ab}(T)$, $\Delta S^{o}_{An-Ab}(T)$, and $\Delta V^{o}_{T\ An-Ab}$ correspond to the difference between the standard state enthalpy, entropy, and volume of fusion of pure An and Ab components, respectively. Eq. (27) is solved by interpolating different thermochemical data from literature (i.e., Table 1 from Glazner, 1984, Table 1 from Lange et al., 2009, Table 1 from Waters and Lange, 2015, and Table 2 from Namur et al., 2012; Supplementary Material 6). Permutation of these data produces an almost negligible variation for $\Delta G^{o}_{An-Ab}(T)$ as a function of *T* that never exceeds ~6%. Ab and An melting curves resulting from Gibbs free energies of pure components substantially overlap with those reported in previous works (i.e., Fig. 5 in Lange et al., 2009 and Fig. 3 in Namur et al., 2012) and for this reason are not presented here. At the investigated *P-T* conditions, we calculate that Eq. (21) for pure An and Ab components returns $\Delta G^{o}_{An-Ab}(P,T)$ from 25.9 to 28.4 kJ mol^{-1}, $\Delta G^{o}_{An-Ab}(T)$ from 28.6 to 27.8 kJ mol^{-1}, and $\Delta G^{o}_{An-Ab}(P)$ from −0.18 to −1.88 kJ mol^{-1}. Notably, within the *P* range of 30–300 MPa, the energetic contribution of $\int_1^P \Delta V^{o}_{T\ An-Ab}(P)dP$ leads to the plot of $\Delta G^{o}_{An-Ab}(T)/RT$ against $\Delta G^{o}_{An-Ab}(P,T)/RT$ which shows a maximum deviation of ~8% from the one-to-one regression line (Supplementary Material 6). Because $\Delta G^{o}_{An-Ab}(T) >> \Delta G^{o}_{An-Ab}(P)$ and $\Delta G^{o}_{An-Ab}(P,T) \approx \Delta G^{o}_{An-Ab}(T)$, the An-Ab exchange reaction is weakly sensitive to pressure changes during plagioclase saturation at crustal depths (cf. Lange et al., 2009). It is therefore not surprising that the uncertainty of plagioclase-based barometers is much greater than the dynamics of magma transport within volcanic conduits, corresponding to ±380 MPa (i.e., a depth uncertainty of ±17 km presuming a continental crust density of 2.7 g/cm^3) for barometers calibrated by global regression analysis of 727 literature data (see Fig. 5 in the review study of Putirka, 2008).

5.2. Anorthite-albite melt activities and the role of H_2O^{melt}

The solution of Eq. (26) requires that activity-composition relations of An and Ab in both plagioclase and melt phases are calculated by considering the ideal and non-ideal parts of $ln(K^{eq}_{An-Ab})$:

$$ln(K^{eq}_{An-Ab}) = \left[ln\left(\frac{X^{pl}_{An}}{X^{pl}_{Ab}}\right)^{ideal} + ln\left(\frac{\gamma^{pl}_{An}}{\gamma^{pl}_{Ab}}\right)^{non-ideal}\right] - \left[ln\left(\frac{X^{melt}_{An}}{X^{melt}_{Ab}}\right)^{ideal} + ln\left(\frac{\gamma^{melt}_{An}}{\gamma^{melt}_{Ab}}\right)^{non-ideal}\right] \quad (28)$$

where $K^{ideal}_{An-Ab} = \left(\frac{X^{pl}_{An}X^{melt}_{Ab}}{X^{pl}_{Ab}X^{melt}_{An}}\right)^{ideal}$ and $K^{non-ideal}_{An-Ab} = \left(\frac{\gamma^{pl}_{An}\gamma^{melt}_{Ab}}{\gamma^{pl}_{Ab}\gamma^{melt}_{An}}\right)^{non-ideal}$. The non-ideal part of K^{eq}_{An-Ab} represents the excess Gibbs free energy (ΔG_{ex}) that incorporates the deviation from ideality for the solution of An and Ab components in both phases (Putirka, 2017).

The solid solution of plagioclase is not ideal due to the occurrence of two structural states and different degrees of Si—Al ordering in tetrahedral coordination (Carpenter, 1988). However, at magmatic temperatures, activity-relation models for plagioclase approximate the condition where An-Ab solid solution can be considered to mix ideally on one site per 8-oxygen formula unit. This implies that $a^{pl}_{An} \cong (X^{pl}_{An})^{ideal}$ and $a^{pl}_{Ab} \cong (X^{pl}_{Ab})^{ideal}$ with quantities that never differ by more than 10%, as documented by Glazner (1984) and Namur et al. (2012).

For the melt counterpart, ideal interactions of oxide components are calculated according to Carmichael et al. (1977):

$$(X^{melt}_{An})^{ideal} = 64.000(X^{melt}_{CaO})(X^{melt}_{Al2O3})(X^{melt}_{SiO2})^2 \quad (29)$$

$$(X^{melt}_{Ab})^{ideal} = 18.963(X^{melt}_{Na2O})^{0.5}(X^{melt}_{Al2O3})^{0.5}(X^{melt}_{SiO2})^3 \quad (30)$$

An early attempt to develop empirical equations for γ^{melt}_{An} and γ^{melt}_{Ab} as a function of oxide components in the melt is reported in Glazner (1984) using 101 experimental plagioclase-melt pairs from basaltic to dacitic compositions equilibrated at $P = 0.1$–1500 MPa, $T \approx 1060$–1400 °C, and $fO_2 \leq$ QFM under anhydrous conditions. The final expressions for the activity coefficients (see Tables 3 and 4 in Glazner, 1984) are similar to a Margules power-series expansion for excess Gibbs free energy $\Delta G_{ex} = f(W)$, where *W* is the Margules interaction parameter. It must be noted that this type of equation does not provide a direct measure of the activity of oxide component, as the estimated quantity *W* is proportional but not identical to the true melt activity. Hence the final form of $\Delta G_{ex} = f(W)$ can be generally defined as activity model. Application to our experiments (Fig. 8a,b) returns modest regression statistics for the coefficient of determination ($R^2_{An} = 0.65$ and $R^2_{Ab} = 0.52$) and standard error of estimate ($SEE_{An} = 0.22$ and $SEE_{Ab} = 0.21$). The low accuracy of the polynomial function is essentially due to the absence of mafic alkaline compositions in the calibration data set of Glazner (1984), which includes only melts with tholeiitic and calc-alkaline affinities. The important aspect to keep in mind is that Margules interaction parameters are defined from experimental data on coexisting plagioclase-melt pairs. Once calibrated, these interaction parameters describe in first approximation ΔG_{ex} of a multicomponent system bounded by the *P-T-X* conditions of the calibration data (Ghiorso et al., 1983).

The most recent model of Namur et al. (2012) is based on a large data set of 530 plagioclase-melt pairs obtained for picrobasaltic to rhyolitic compositions equilibrated under anhydrous conditions at $P = 0.1$ MPa, $T \approx 1000$–1350 °C, and $fO_2 \leq$ QFM. The calibration data set includes alkaline mafic compositions, such as alkaline basalts, tephrites, trachybasalts, basaltic trachyandesites, and trachyandesites. Through the regression analysis of anhydrous melt components expressed as cation proportions on an 8-oxygen basis, Namur et al. (2012) obtains two

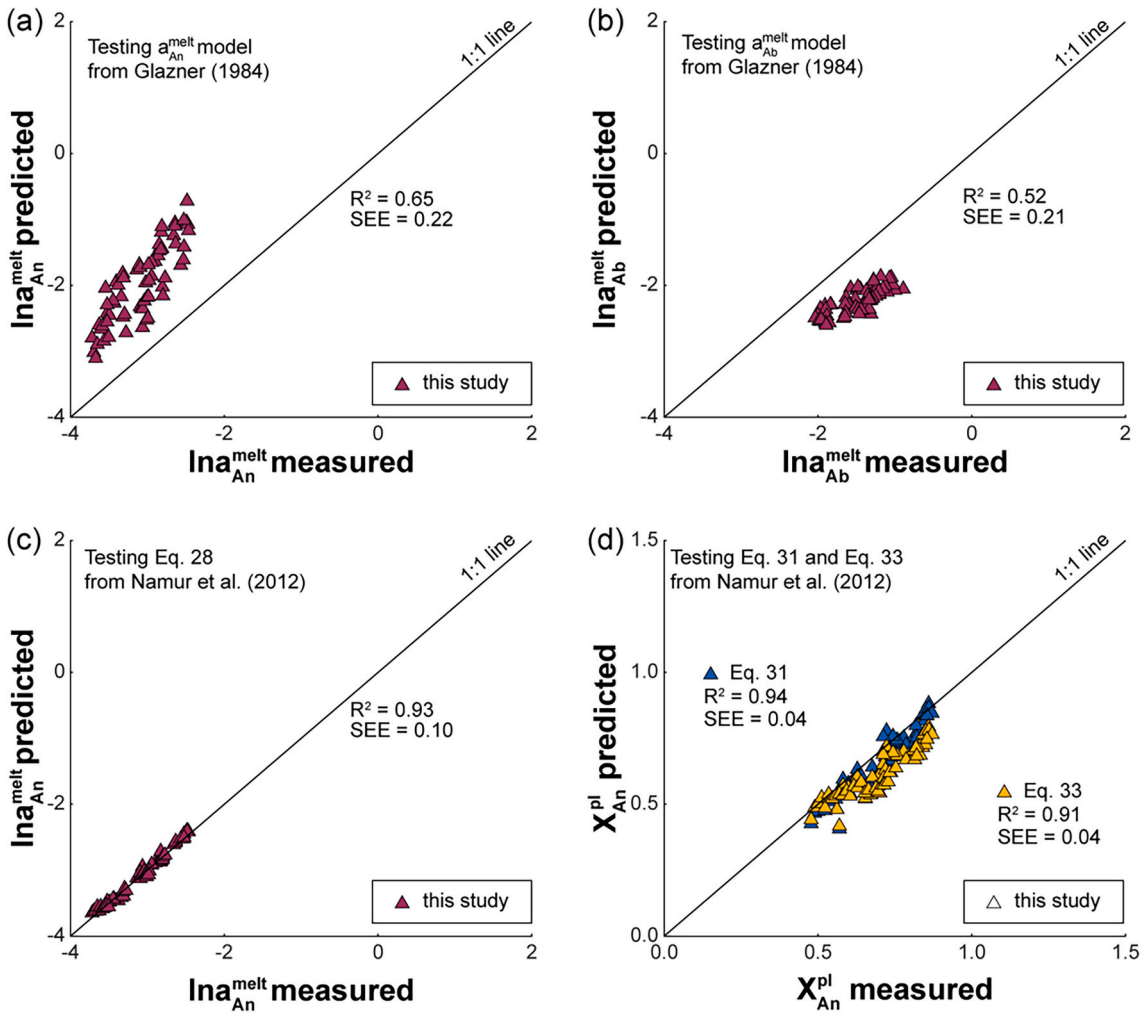

Fig. 8. Plot of measured against predicted values of $\ln(a_{An}^{melt})$ (a) and $\ln(a_{Ab}^{melt})$ (b) using the model of Glazner (1984). Plot of measured against predicted values of $\ln(a_{An}^{melt})$ using Eq. 28 from Namur et al. (2012) (c). Plot of measured against predicted values of X_{An}^{pl} using Eq. (31) and Eq. (33) from Namur et al. (2012) (d).

empirical models for the estimate of $\ln(a_{An}^{melt})$ and X_{An}^{pl} [i.e., Eq. (28) and Eq. (31), respectively, in Namur et al., 2012]. An additional anhydrous model for calculating X_{An}^{pl} is specific to mafic–ultramafic melts and includes a subset of 298 melt compositions [i.e., Eq. (33) in Namur et al., 2012]. Although all these models were derived on an anhydrous basis, we found successful application to hydrous mafic alkaline melt compositions [$^{Eq.\ (28)}R^2 = 0.93$, $^{Eq.\ (31)}R^2 = 0.94$, and $^{Eq.\ (33)}R^2 = 0.91$, and $^{Eq.\ (28)}SEE = 0.10$, $^{Eq.\ (31)}SEE = 0.04$, and $^{Eq.\ (33)}SEE = 0.04$; Fig. 8c,d]. In principle, the effect of dissolved water is to decrease the activity of silica in the melt and the saturation surface of plagioclase (Ghiorso et al., 1983). However, for low to moderate amounts of dissolved water in the melt (i.e., $H_2O^{melt} \approx 0.0$–4.4 wt%; Supplementary Materials 1 and 2), the magnitude of this effect is overwhelmingly dominated by the variation of anhydrous melt components as a function of T, giving reason for the very good regression statistics of the anhydrous models proposed by Namur et al. (2012) (Fig. 8c,d).

The composition-related non-ideality of multicomponent silicate melt can be thermodynamically modeled using a symmetric regular solution type equation (Nicholls, 1980; Ghiorso and Carmichael, 1980; Ghiorso et al., 1983). Among the numerous models from the literature to calculate the activity coefficient of a component as a function of W in a multicomponent solution, we adopt the expression (Ghiorso and Carmichael, 1980):

$$RTln\gamma_k^{melt} = \sum_{i=1}^{n} W_{ik} X_i^{2\ melt} + \sum_{i=2}^{n} X_i^{melt} \sum_{j=1}^{i-1} \left(W_{ik} + W_{kj} - W_{ij}\right) X_j^{melt}; i, j \neq k \quad (31)$$

Following Nicholls (1980), we choose an algebraically simple form for calculating the effect of one melt component on another by expressing oxides as mole fractions and using these quantities to represent melt composition. Glazner (1984) emphasizes that oxide mole fractions can be used to describe melt composition without further manipulations, as they represent the simplest independently variable components in the melt. Values of γ_k^{melt} are calculated for the appropriate oxide component of the melt through experimental compositions from this study, whereas the binary interaction coefficient W is assumed as a constant independent of the P-T-X conditions. The rationale behind this choice is that Eq. (26) was originally designed for olivine- and plagioclase-melt equilibria in pressure-temperature regions typical of basaltic systems (Ghiorso and Carmichael, 1980). All mixing properties of oxide components are determined on an anhydrous basis and then employed to estimate the partial molar free energies of An and Ab. The partial molar excess Gibbs free energies predicted by Eq. (26) are also interpreted by Ghiorso and Carmichael (1980) as a potential thermometer for plagioclase in equilibrium with both anhydrous and hydrous melts.

To obtain a thermodynamic description for the activity coefficients of An and Ab components in the melt with Eq. (31), we derive values of

γ_{An}^{melt} and γ_{Ab}^{melt} by considering the stoichiometric proportions of $CaAl_2Si_2O_8$ and $NaAlSi_3O_8$ as (Nicholls, 1980):

$$CaO^{melt} + Al_2O_3{}^{melt} + 2SiO_2{}^{melt} = CaAl_2Si_2O_8{}^{melt} \quad (32)$$

$$0.5Na_2O^{melt} + 0.5Al_2O_3{}^{melt} + 3SiO_2{}^{melt} = NaAlSi_3O_8{}^{melt} \quad (33)$$

Owing to the very poor correlation between H_2O^{melt} and plagioclase-melt components in mafic alkaline systems (Figs. 4 and 6), we assume for the moment that the effect of water solution does not substantially impact the melt configurational excess energy of mixing (i.e., nearly ideal solution model). Recalling that $a_{\mathrm{An\ or\ Ab}}^{melt} = X_{\mathrm{An\ or\ Ab}}^{melt}\gamma_{\mathrm{An\ or\ Ab}}^{melt}$, Eq. (19) is rearranged as:

$$ln\left(a_{\mathrm{An\ or\ Ab}}^{melt}\right)^{measured} = ln\left(a_{\mathrm{An\ or\ Ab}}^{pl}\right) - \frac{\Delta G_{An\ or\ Ab}^{o}(P,T)}{RT} \quad (34)$$

Margules interaction parameters of Eq. (31) are calculated through a stepwise linear least square regression of experimental data from this study, which is the same procedure reported in Kress and Carmichael (1988). Activity coefficients from Eq. (32) ($\gamma_{An}^{melt} = \gamma_{CaO}^{melt} + \gamma_{Al2O3}^{melt} + 2\gamma_{SiO2}^{melt}$) and Eq. (33) ($\gamma_{Ab}^{melt} = 0.5\gamma_{Na2O}^{melt} + 0.5\gamma_{Al2O3}^{melt} + 3\gamma_{SiO2}^{melt}$) are then used to determine $\ln(a_{An}^{melt})^{predicted}$ and $\ln(a_{Ab}^{melt})^{predicted}$, respectively. The best estimates of the model parameters and the goodness of the calculation are quantitatively evaluated by minimization of the Pearson's chi-square statistic (Harris and Kanji, 1983):

$$\chi_p^2 = \sum_{i=1}^{n} \frac{\left[ln\left(a_{\mathrm{Ab\ or\ An}}^{melt}\right)^{measured} - ln\left(a_{\mathrm{Ab\ or\ An}}^{melt}\right)^{predicted}\right]}{ln\left(a_{\mathrm{Ab\ or\ An}}^{melt}\right)^{measured}} \quad (35)$$

Multivariate analysis is also performed to prevent model instability caused by data overfitting and/or multicollinearity. All values of W for γ_{An}^{melt} and γ_{Ab}^{melt} are reported in Supplementary Material 6, in which binary interaction parameters identified as statistically insignificant predictors are set to zero. Fig. 9a shows alignment between measured and predicted An and Ab activities in the melt [i.e., $\ln(a_{\mathrm{An\ or\ Ab}}^{melt})^{measured}$ against $\ln(a_{\mathrm{An\ or\ Ab}}^{melt})^{predicted}$], with fairly good regression statistics of $R_{aAn}^2 = 0.93$, $R_{aAb}^2 = 0.93$, $SEE_{aAn} = 0.07$, and $SEE_{aAb} = 0.08$.

The effect of dissolved water on the activity coefficient calculation is tested in relation to the dissociation reaction of water in the melt (Stolper, 1982):

$$H_2O_{molecular} + O^o = 2OH^- \quad (36)$$

where $H_2O_{molecular}$, O^o, and OH^- refers to the molecular water, bridging oxygens, and OH^- group attached to a silicate polymer. Since liquidus temperature is a nonlinear function of water concentration, complex activity-composition relations are generally determined for hydrous silicate melts (e.g., Burnham, 1975). Margules interaction parameters are considered for describing the non-ideality of water dissolution in the melt by incorporating into Eq. (26) the thermodynamic expression:

$$W_{H2O}X_{H2O}^{melt} + W_{H2O^2}X_{H2O}^{2\ melt} + W_{H2O^{0.5}}X_{H2O}^{0.5\ melt} \quad (37)$$

where $W_{H2O}X_{H2O}$ represents the total amount of water dissolved in the melt, $W_{H2O^2}X_{H2O}^2$ refers to $H_2O_{molecular}$, and $W_{H2O^{0.5}}X_{H2O}^{0.5}$ is a proxy for OH^- (see Ueki et al., 2020 for a more comprehensive description of water-related terms). Results from thermodynamic calculations are reported in Supplementary Material 6. However, Fig. 9b shows that the speciation of water does not offer any improvement in the ability prediction of An and Ab activities in the melt ($R_{aAn}^2 = 0.93$, $R_{aAb}^2 = 0.92$, $SEE_{aAn} = 0.08$, and $SEE_{aAb} = 0.08$), thereby emphasizing the subordinate role of water on plagioclase-melt equilibria at the experimental conditions investigated here (compare Figs. 3, 5, and 8c,d).

Thermodynamic calculations are also verified by multivariate descriptive statistics derived for the parameters: 1) H_2O^{melt}, 2) T, 3) plagioclase components [i.e., $\ln(X_{An}^{pl})$ and $\ln(X_{Ab}^{pl})$], 4) melt components [i.e., $\ln(X_i^{melt})$ and related cross-product terms as $\ln(X_i^{melt}X_i^{melt})$, where i is the cations of interest], 5) plagioclase-melt partition and exchange partition coefficients [i.e., $\ln(K_{An}^{pl-melt})$, $\ln(K_{Ab}^{pl-melt})$, and $\ln(Kd_{An-Ab}^{pl-melt})$], and 6) plagioclase-melt equilibrium constants [i.e., $\ln(K_{An}^{eq})$, $\ln(K_{Ab}^{eq})$, and $\ln(K_{An-Ab}^{eq})$]. The resulting correlation matrix is reported in Supplementary Material 7. Extremely high *p-values* are obtained for T (0.71), $\ln(K_{An}^{pl-melt})$ (0.71), $\ln(K_{An-Ab}^{pl-melt})$ (0.39), $\ln(K_{An}^{eq})$ (0.70), and $\ln(K_{Ab}^{eq})$ (0.70), as these parameters are not statistically significant for the description of H_2O^{melt}. Also, the absolute value of *Pearson's r* does not satisfy the statistical threshold of 0.60 for $\ln(K_{Ab}^{pl-melt})$ (0.24), $\ln(K_{An-Ab}^{eq})$ (0.43), $\ln(X_{An}^{pl})$ (0.39), and $\ln(X_{Ab}^{pl})$ (0.38). Multivariate analysis confirms the weak correlation between H_2O^{melt} and $Kd_{An-Ab}^{pl-melt}$ (Fig. 5), attesting the negligible effect of dissolved water on An and Ab melt activities (Figs. 8c, d and 9a,b). By regressing H_2O^{melt} against the best predictors (i.e., *p-values* < 0.05 and *Pearson's r* > 0.60; Supplementary Material 7) and testing for the absence of multicollinearity ($VIF < 10$), we cannot derive any predictive model performing better than plagioclase-based hygrometers published in literature that comparatively return a conservative uncertainty nearly close to ~1.1 wt%. In particular, Eq. (H) (uncertainty ±1.1 wt% H_2O^{melt}) from Putirka (2005), Eq. (25b) (uncertainty ±1.1 wt% H_2O^{melt}) from Putirka (2008), Eq. (25) (uncertainty

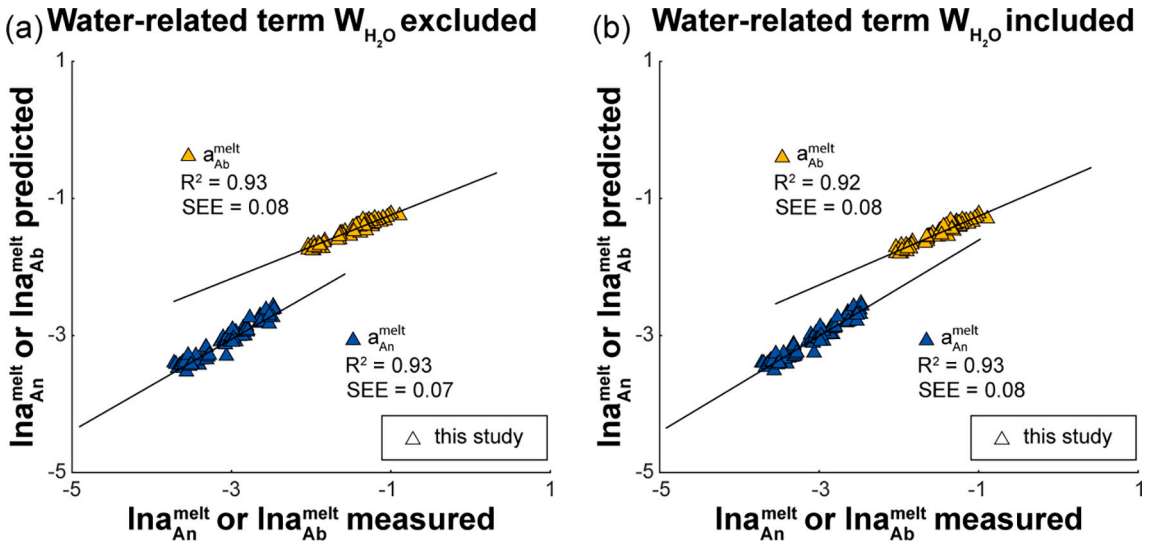

Fig. 9. Plot of measured against predicted values of $\ln(a_{\mathrm{An\ or\ Ab}}^{melt})$ by excluding (a) and including (b) the water-related Margules interaction parameters from Ueki et al. (2020).

±0.32 wt% H_2O^{melt}) from Lange et al. (2009), and Eq. (14) (uncertainty ±0.35 wt% H_2O^{melt}) from Waters and Lange (2015) perform moderately well with the mafic alkaline data set, yielding $^{Eq.\ (H)}SEE = 1.2$ wt%, $^{Eq.\ (25b)}SEE = 1.1$ wt%, $^{Eq.\ (25)}SEE = 1.1$ wt%, and $^{Eq.\ (14)}SEE = 1.0$ wt%, respectively (Supplementary Material 7).

5.3. Plagioclase-based thermometry

For the purpose of modeling plagioclase crystallization conditions, activities of An and Ab in the melt are parameterized in a simpler and more tractable regression form, which includes first-order and second-order product terms for *n* oxide components in the melt (cf. Glazner, 1984; Namur et al., 2012; Putirka, 2017):

$$ln\left(a^{melt}_{\text{An or Ab}}\right)^{measured} = f\left(\sum_{i=1}^{n} X^{melt}_i + X^{melt}_i \sum_{i=1}^{n} X^{melt}_i\right) \quad (38)$$

Correlation matrices for these activity terms are reported in Supplementary Material 8 and weighted multiple linear regression analysis returns:

$$\begin{aligned} ln\left(a^{melt}_{\text{An}}\right) = {} & -3.67(\pm 0.75) + 0.72(\pm 0.30)X^{melt}_{Si} + 258.51(\pm 67.71)X^{melt}_{Ti} \\ & - 13.21(\pm 7.38)X^{melt}_{Fe} - 65.02(\pm 6.13)X^{melt}_{Mg} + 32.61(\\ & \pm 1.75)X^{melt}_{Ca} - 2864.94(\pm 910.40)X^{melt}_{Ti}X^{melt}_{Fe} + 75.17(\\ & \pm 14.52)X^{melt}_{Al}X^{melt}_{Fe} + 57.57(\pm 18.51)X^{melt}_{Al}X^{melt}_{Mg} + 45.95(\\ & \pm 5.43)X^{melt}_{Fe}X^{melt}_{Na} + 204.61(\pm 47.20)X^{2\ melt}_{Mg} - 88.81(\\ & \pm 9.35)X^{2\ melt}_{Ca} \end{aligned} \quad (39)$$

$$\begin{aligned} ln\left(a^{melt}_{\text{Ab}}\right) = {} & -2.74(\pm 0.16) + 10.31(\pm 5.50)X^{melt}_{Mg} + 8.85(\pm 1.41)X^{melt}_{Ca} \\ & + 5.06(\pm 2.69)X^{melt}_{Na} + 322.61(\pm 187.37)X^{melt}_{Ti}X^{melt}_{Mg} + 30.47(\\ & \pm 4.55)X^{melt}_{Al}X^{melt}_{Ca} - 37.24(\pm 9.50)X^{melt}_{Fe}X^{melt}_{Na} - 146.32(\\ & \pm 41.84)X^{2\ melt}_{Mg} - 34.66(\pm 8.51)X^{2\ melt}_{Ca} - 38.58(\pm 17.90)X^{2\ melt}_{Na} \end{aligned} \quad (40)$$

The very good regression statistics derived for Eq. (39) ($R^2_{aAn} = 0.99$) and Eq. (40) ($R^2_{aAb} = 0.99$) reflect the high accuracy of the models ($SEE_{aAn} = 0.004$ and $SEE_{aAb} = 0.003$). Although several filters are used to prevent data overfitting and multicollinearity, regression statistics derived for Eq. (39) and Eq. (40) are slightly better than those obtained from the solution of Eq. (31) using Margules interaction parameters. This is confirmed by thermodynamic calculations performed by Putirka (2017) on An and Ab activity composition relations. The author tests different plagioclase and melt activity models from literature by regressing 1 bar anhydrous experiments to calculate values approaching to the calorimetric measurement of $\Delta H^{fusion}_{An} = 135 \pm 10$ kJ mol^{-1}. By performing cyclic permutations, Putirka (2017) finds that application of different activity models produces very contrasting ΔH^{fusion}_{An} values bounded between 18.7 and 139.6 kJ mol^{-1}, with the majority of data within the range of 18.7–55.2 kJ mol^{-1} (see Table 4 in Putirka, 2017). By propagating errors associated with Eq. (31) and Eq. (39), regression fit of our data returns a similar range of 17.2–50.3 kJ mol^{-1}. It appears that the empirical solution of K^{eq}_{An} leads to ΔH^{fusion}_{An} values much lower than the calorimetric measurement. As explained by Putirka (2017), there is still poor understanding of crystal and melt component activities due to the fact that regression analysis of experimental data fails in determining unequivocal thermodynamic parameters. Regression coefficients are strongly sensitive to the type and number of independent variables and the calibration data used for the regression analysis. As a consequence, although activity models rely on solid thermodynamic principles, their incorporation in thermometers, barometers, and hygrometers may strongly impair the ability prediction of the models (Putirka, 2017).

To calibrate a plagioclase-based thermometer specific to mafic alkaline compositions, we take advantage of the close relation between $K^{eq}_{\text{An-Ab}}$ and *T*, by adopting the thermodynamic expression recommended in Putirka's works and derived by rearranging Eq. (26) (see Putirka et al., 1996; Putirka, 2005; Putirka, 2008; Putirka, 2017):

$$\frac{10^4}{T\ (K)} = aK^{eq}_{\text{An-Ab}} + b + cP + dln\left(\Theta^{melt}_1\right) + e\left(\Theta^{pl}_1\right)\ldots + Nln\left(\Theta^{melt}_n, \Theta^{pl}_n\right) \quad (41)$$

The pressure term *cP* can be eluded owing to the negligible effect of $\Delta V^o_{T\ An}(P)dP$ on the An-Ab exchange reaction. The parameter $Nln(\Theta^{melt}_n, \Theta^{pl}_n)$ accounts for the non-ideal behavior of $K^{eq}_{\text{An-Ab}}$ due to mixing and interaction between An and Ab chemical components. $Nln(\Theta^{melt}_n, \Theta^{pl}_n)$ represents a pseudo-activity modifying term empirically derived by regression analysis of experimental data (Putirka et al., 1996). *N* may or may not be proportional to the activity coefficient of the component of interest (Putirka, 2008, 2017). If necessary, two components with the same activity coefficient are also combined as cross-product terms to provide the best compositional correction (Supplementary Material 9). Assuming $a^{pl}_{\text{An}} \cong X^{pl}_{\text{An}}$ and $a^{pl}_{\text{Ab}} \cong X^{pl}_{\text{Ab}}$, we calculate $K^{eq}_{\text{An-Ab}}$ through Eq. (39) and Eq. (40). *VIF* analysis indicates that most of melt components are embodied in the calculation of $K^{eq}_{\text{An-Ab}}$. Only X^{pl}_{An} and X^{pl}_{Ab} for plagioclase and a few melt (X^{melt}_{Si}, X^{melt}_{Ti}, X^{melt}_{Fe}, X^{melt}_{Mg}, X^{melt}_{Ca}, $X^{melt}_{\text{Ti}}X^{melt}_{\text{Al}}$, and $X^{melt}_{\text{Fe}}X^{melt}_{\text{K}}$) components are not affected by multicollinearity (*VIF* < 10). Further application of *Mallows' Cp* lowers the number of predictors to X^{pl}_{An} and X^{pl}_{Ab}, as the use of these components is enough to guarantee unbiased regression coefficients. Weighted multiple linear regression analysis yields the following thermometric equation:

$$\begin{aligned} \frac{10^4}{T\ (K)} = {} & 6.39\ (\pm 0.19) + 0.68\ (\pm 0.05)ln\left(\frac{X^{pl}_{An}}{a^{melt}_{An}\ from\ Eq.(39)}\right. \\ & \left. \times \frac{a^{melt}_{Ab}\ from\ Eq.(40)}{X^{pl}_{Ab}}\right) - 1.06\ (\pm 0.19)lnX^{pl}_{An} + 0.81(\pm 0.09)lnX^{pl}_{Ab} \end{aligned} \quad (42)$$

Eq. (42) reproduces *T* with $R^2 = 0.80$ and $SEE = 11$ °C. The incorporation of H_2O^{melt} parameter in Eq. (42) offers a mediocre improvement of ±3 °C ($R^2 = 0.91$ and $SEE = 11$ °C), emphasizing the subordinate influence of water on $K^{eq}_{\text{An-Ab}}$ relative to the stronger effects of melt and temperature changes. In Fig. 10, the predictive power of Eq. (42) is compared with those of plagioclase-based thermometers from Putirka (2005) [Eq. (A) and Eq. (D)], Putirka (2008) [Eq. (24a) and Eq. (26)], and Putirka (2017) [Eq. (27a), Eq. (27b), and Eq. (27c)]. It is worth stressing that these models depend on *P* and/or H_2O^{melt} as input parameters. For this comparison, we calculate the difference between *T* measured from the experimental data set minus *T* predicted by each different model, together with the tested standard error of estimate. As a general rule, the precision of previous models derived by regression of large data sets is systematically lower than that of Eq. (42) obtained for a subset of mafic alkaline data. Barometers, thermometers, and hygrometers obtained from restricted ranges of compositions and conditions more closely describe the variance of the calibration data set (Masotta et al., 2013; Mollo et al., 2015c, 2018). However, we note that $^{Eq.\ (27b)}SEE = 44$ °C and $^{Eq.\ (27c)}SEE = 57$ °C obtained for mafic alkaline data are ~10 °C lower than $^{Eq.\ (27b)}SEE = 55$ °C and $^{Eq.\ (27b)}SEE = 67$ °C originally derived by Putirka (2017). Analogously, $^{Eq.\ (26)}SEE = 29$ °C measured in this study is better than $^{Eq.\ (26)}SEE = 37$ °C tested by Putirka (2008). Although some advantages can be envisaged in the use of *P*-H_2O^{melt}-independent Eq. (42), the disadvantage of thermometers derived from a restricted data set is that they cannot be safely extrapolated to a broad range of compositions and crystallization conditions without returning systematic errors (see for example Masotta et al., 2013; Mollo et al., 2015c, 2018). For volcanic settings compositionally different from Stromboli and Mt. Etna, global regression models reported in Putirka (2008, 2017) are still recommended as their regression parameters and coefficients rely on large calibration data sets, including up to ~1200 plagioclase-melt pairs equilibrated at *P*, *T*, and H_2O^{melt} up

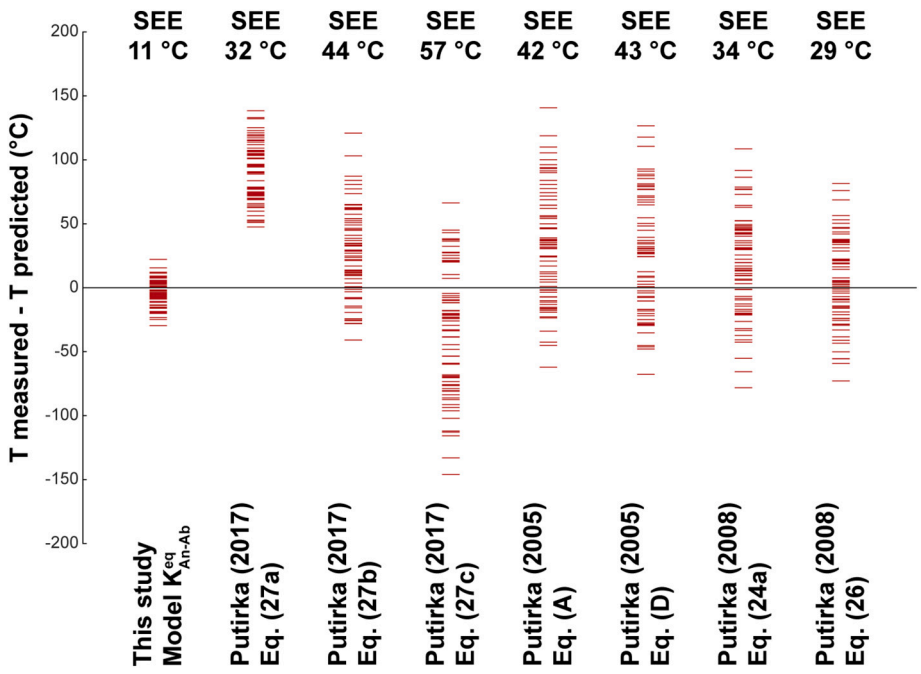

Fig. 10. Plot of measured against predicted values of temperature from different plagioclase-based thermometric models. Eq. (42) from this study is compared with Eq. (A) and Eq. (D) from Putirka (2005), Eq. (24a) and Eq. (26) from Putirka (2008), Eq. (27a), Eq. (27b) and Eq. (27c) from Putirka (2017). SEE refers to the standard error of estimate resulting from the model calibration.

to ~2.7 GPa, ~1430 °C, and ~ 13 wt%, respectively. A virtue of these models is the inclusion of tholeiitic and calc-alkaline compositions for which water has a strong non-linear effect on the liquidus depression of both olivine and plagioclase, thus offering a more accurate description for the marked compositional change of the melt in equilibrium with variable mineral assemblages as a function of dissolved water (Almeev et al., 2012 and references therein).

The enduring paradigm of estimating mineral saturation temperature under natural crystallization conditions is that we do not know a priori the melt composition in equilibrium with a specific single crystal and/or crystal zone. As a first approximation, the composition of matrix melt can be tentatively paired with that of plagioclase phenocryst rim if it is verified that cooling and decompression processes do not cause microlite crystallization at the time of eruption. Alternatively, the bulk rock analysis can be equilibrated with the anorthitic plagioclase core, if feldspar is recognized as the early liquidus phase. However, this is a rare event for mafic alkaline magmas where plagioclase crystallize cotectically with clinopyroxene (Armienti et al., 2013; Mollo et al., 2015a). In volcanic settings, the occurrence of residual melts is generally sporadic due to abundant *syn*- and post-eruptive crystallization of matrix minerals. Moreover, open-system processes such as magma mixing, mush cannibalism, and hybridization reactions cause juxtaposition of plagioclase crystals with very different growth histories, even at the small scale of a thin section (Cashman and Blundy, 2013). For this reason, recognition of the correct chemical correspondence between a variably zoned plagioclase and melt composition it is not a trivial task, essentially in relation to the polybaric-polythermal transfer of magma through compositionally distinct reservoirs and the kinetic growth of crystals (Mollo et al., 2011; Humphreys et al., 2016). To obviate this issue, plagioclase-melt equilibrium can be restored by 1) mass balances in which aliquots of representative mineral phases are subtracted/added back to the bulk rock analysis and 2) by testing different more or less differentiated bulk rock analyses representative of the overall magma evolutionary path of the eruptive period of interest (e.g., Armienti et al., 2013; Mollo et al., 2018). As illustrated above, predictive models based on X^{pl}_{An} [i.e., Eq. (31) and Eq. (33)] of Namur et al. (2012) recover plagioclase-melt equilibrium with a satisfactory uncertainty of ±0.04 (Fig. 8). However, by performing correlation analysis on mafic alkaline data (Supplementary Material 10), we identify first-order and second-order compositional terms that are more tightly correlated with X^{pl}_{An}:

$$X^{pl}_{An} = 2.41(\pm 0.71) - \frac{1800(\pm 521)}{T} + 0.98(\pm 0.33)X^{melt}_{Ti} - 0.58(\pm 0.16)X^{melt}_{Ti}X^{melt}_{Mg} - 0.17(\pm 0.06)X^{melt}_{Fe}X^{melt}_{Na} + 0.40(\pm 0.05)X^{melt}_{Mg}X^{melt}_{Ca} \quad (43)$$

This refined equilibrium model is associated with $R^2_{XAn} = 0.94$ and $SEE_{XAn} = 0.02$. For plagioclase in thermodynamic equilibrium with the host melt, the difference (Δ) between X^{pl}_{An} predicted by Eq. (43) and X^{pl}_{An} measured in plagioclase should be equal to zero. But such a theoretical value does not consider the analytical uncertainty associated with major oxide analysis and error propagation in the estimate of X^{pl}_{An}. In conformity with other equilibrium models (e.g., Putirka et al., 1996; Masotta et al., 2013; Mollo et al., 2013), achievement of near-equilibrium crystallization can be expected for ΔX^{pl}_{An} within the calibration error of ±0.02 obtained by weighted multiple regression analysis of the mafic alkaline data set. We report in Supplementary Material 11 an EXCEL spreadsheet and a MATLAB code to model intracrystalline heterogeneities in plagioclase as a function of temperature and melt-water concentration. For this purpose, thermometric and equilibrium equations from this study [i.e., Eq. (42) and Eq. (43), respectively] are interpolated with previous hygrometric (Putirka, 2005, 2008; Lange et al., 2009; Waters and Lange, 2015) and equilibrium (Namur et al., 2012) equations from the literature.

6. Interpreting T and H_2O^{melt} in zoned plagioclase crystals

Compositional zoning patterns in plagioclase crystals are routinely used by petrologists and volcanologists to estimate the intensive variables governing magma crystallization at pre- and syn-eruptive conditions (e.g., Humphreys et al., 2016; Crabtree and Lange, 2011; Cashman and Blundy, 2013). Here we focus on plagioclase phenocrysts from eight eruptive products representative of normal (24/5/2013, 26/11/2019, and 10/10/2021), major, (8/11/2009, 23/10/2017, and 19/7/2020), and paroxysmal (15/3/2007 and 3/7/2019) explosions at Stromboli in

the period from March 2007 to October 2021. Plagioclase phenocrysts from different eruptions are texturally and compositionally similar, as described in Supplementary Material 12. Following the classification scheme proposed by Landi et al. (2004), crystal zoning patterns can be categorized into four textural domains:

1) subrounded corroded cores (SCC) showing prevalent patchy textures. SCC have anorthite-bytownite compositions, with average An^{pl} = 81 mol% and $\sigma = \pm 3$ mol%, where σ refers to the standard deviation of An^{pl};
2) sieve-textured concentric layers (STCL) showing abundant micrometric glass inclusions. STCL overgrow on dissolution surfaces that are characterized by angular unconformities and crenulated margins. The thickness of each layer is variable from ~10 to ~100 μm. The composition is anorthite-bytownite, with average An^{pl} = 78 mol% and $\sigma = \pm 5$ mol%;
3) oscillatory-zoned concentric layers (OZCL) developing as low amplitude-high frequency oscillatory patterns free of glass inclusions, with little An^{pl} variations ($\Delta An^{pl} \leq 4$ mol%) and zone widths of 1–5 μm. The composition is bytownite-labradorite, with average An^{pl} = 67 mol% and $\sigma = \pm 3$ mol%. Most of the plagioclase phenocryst mantles consist of alternating bands of An-poor OZCL and An-rich STCL domains. Sometimes, OZCL are partly corroded by STCL via the formation of irregular resorption-regrowth An-rich surfaces that crosscut the inner and more An-poor oscillatory zoning patterns;
4) overgrowth rims (OR) with thickness variable from ~10 to ~60 μm and in direct contact with the matrix glass. OR are characterized by marked evolved compositions, with average $An^{pl} = 65$ mol% and $\sigma = \pm 2$ mol%.

According to Landi et al. (2004), STCL grow on erosional surfaces in plagioclase phenocrysts that involve successive dissolution-crystallization processes via recurrent inputs of hot, volatile-rich *Lp*-magmas rising from depth into the uppermost segment of the feeding system, in which colder and more degassed *Hp*-magmas are stored. In situ trace element and Sr isotope analyses of plagioclase phenocrysts by Francalanci et al. (2005, 2012) point out that STCL-OZCL alternation results from up to ~30% of *Lp-Hp* magma mixing causing significant Sr isotope disequilibrium. In this scenario, SCC are interpreted as relic antecrysts belonging to a crystal mush that developed from older progenitor magmas with high Sr isotope ratios. Hotter and more mafic *Lp*-magmas with low Sr isotope ratios pass through the crystal mush column, cannibalize the antecrysts and then transport them into the *Hp*-reservoir (Francalanci et al., 2005, 2012). Periods of relatively slow growth in the *Hp*-reservoir promote the formation of OZCL via sluggish kinetic effects due to small perturbations in the concentration of the melt next to the plagioclase interface (Landi et al., 2004) and/or crystal convection along small thermal and compositional gradients by continuous *Lp-Hp* magma mixing (Francalanci et al., 2005). The cross-cutting relationships between STCL and OZCL domains record resorption-regrowth events due to recurrent *Lp-Hp* magma mixing in the *Hp*-reservoir. This produces new hybrid magmas with intermediate Sr isotope ratios feeding the growth of STCL by partial dissolution of pre-existing OZCL formed in the *Hp*-reservoir (Francalanci et al., 2005, 2012). OR are strongly depleted in An due to late textural equilibration at low-*T,* low-*P* conditions by abundant magma degassing (Landi et al., 2004), also in accord with in situ Sr isotope analyses suggesting isotopic equilibrium between OR and the glassy groundmass (Francalanci et al., 2012).

Integration of numerical multiphase steady-state modeling (La Spina et al., 2015) and thermodynamic calculations (Landi et al., 2004) indicates that most of plagioclase crystallization takes place at $P \leq 130$ MPa, $T \leq 1135$ °C, and $H_2O^{melt} \leq 2.8$ wt% for $P_{H2O} < P_{total}$ (Landi et al., 2004). Numerical modeling data point out also that the decrease of temperature has a great influence on magma ascent dynamics and is related to a non-isothermal condition along the conduit, as the result of competition between crystallization (heating) and gas expansion (cooling) processes (La Spina et al., 2015). Because crystallization and melt viscosity are both strongly temperature-dependent, these results emphasize that temperature, rather than melt-water content, plays an important role on controlling the volume flow rate and the crystal content of Stromboli magmas at the vent of the conduit. For instance, the mass discharge rate increases by 1) an order of magnitude upon a *T* variation of 30 °C and 2) a factor of ~5 per 1 wt% increase in H_2O^{melt} (La Spina et al., 2015). Also, it is not excluded that the ascent of water-undersaturated *Lp*-magmas from greater depths may lower the saturation surface of plagioclase by promoting the stabilization of An-rich compositions and dissolution of An-poor crystals still surviving within the mush column (Nelson and Montana, 1992; Ginibre and Wörner, 2007).

Through the use of plagioclase-melt models reported in Supplementary Material 11, we estimate *T* from Eq. (42) and H_2O^{melt} from the hygrometers of Putirka (2008) and Waters and Lange (2015) for different textural domains in plagioclase (see Supplementary Material 12). The equilibrium condition between plagioclase and the matrix glass is also tested by employing Eq. (43) to prevent unreliable estimates (cf. Mollo et al., 2011; Humphreys et al., 2016). Results from calculations are displayed in Fig. 11 as violin plots and box plots for An^{pl}, *T*, and H_2O^{melt}. A kernel density estimation is used to visualize the underlying probability density function of each set of data in violin plots, whereas the statistical dispersion of data is illustrated by the box. For *T* and H_2O^{melt} estimates, box plots account for model errors and error propagation effects. Once the *T* uncertainty of ±11 °C from Eq. (42) is propagated into the hygrometric equations, an average percentage error of ~16–19% is associated to each H_2O^{melt} estimate and is in addition to the original calibration errors of the hygrometers (i.e., 1.1 and 0.35 wt% H_2O^{melt} for the model of Putirka, 2008 and Waters and Lange, 2015, respectively). The length of the box represents the interquartile range (*IQR*) extending from the first quartile (25th percentile *Q1*) to the third quartile (75th percentile *Q3*) and whiskers go from each quartile to the minimum or maximum (see Supplementary Material 12). Violin plots show symmetric and asymmetric shapes extending beyond the actual minimum and maximum estimates of *T* and H_2O^{melt}, owing to the fact that kernel density projections are greater than the errors associated with thermometric and hygrometric calculations (Fig. 11). The bandwidth of each violin curve corresponds with the approximate frequency of data in each region and accounts to stretched (small bandwidth) or compressed (large bandwidth) data distributions (Fig. 11). For a given textural domain, we observe that *IQR* from box plots systematically overlap, and no apparent variations can be appreciated from one eruption to another and/or from different types of eruptions (Fig. 11). This indicates that the crystallization history of plagioclase phenocrysts at Stromboli is controlled by steady-state magma dynamics resulting from highly efficient magma mixing and degassing regimes, even if the eruptive style changes from normal to major to paroxysmal events (Petrone et al., 2016, 2018, 2022). According to Di Stefano et al. (2020), continuous injections of mafic *Lp*-magmas mix with the more differentiated mush melts migrating into the shallow reservoir, thus preserving the compositional uniformity of the *Hp*-magma. Differently from olivine and clinopyroxene, plagioclase saturates the basaltic melt at the late stage of crystallization within the uppermost part of the mush (e.g., Di Stefano et al., 2020). As a consequence, zoning patterns in plagioclase phenocrysts from the same textural domain record almost equivalent *T* and H_2O^{melt} conditions due to the steady-state dynamics of an open conduit system undergoing continuous recharge, crystallization, and eruption (Fig. 11).

Box plots of An^{pl} (Fig. 11a) and *T* (Fig. 11b) tend to overlap, showing a pair-wise behavior for SCC + STCL and OZCL + OR. The maximum probability distribution of An^{pl} is embodied within the *Q1-Q3* range (Supplementary Material 12) and corresponds to anorthitic compositions of 78–84 (SCC) and 74–83 (STCL), and 64–70 (OZTL), and 63–67 (OR) mol.% for the 2007–2021 eruptive period. Similarly, we found that

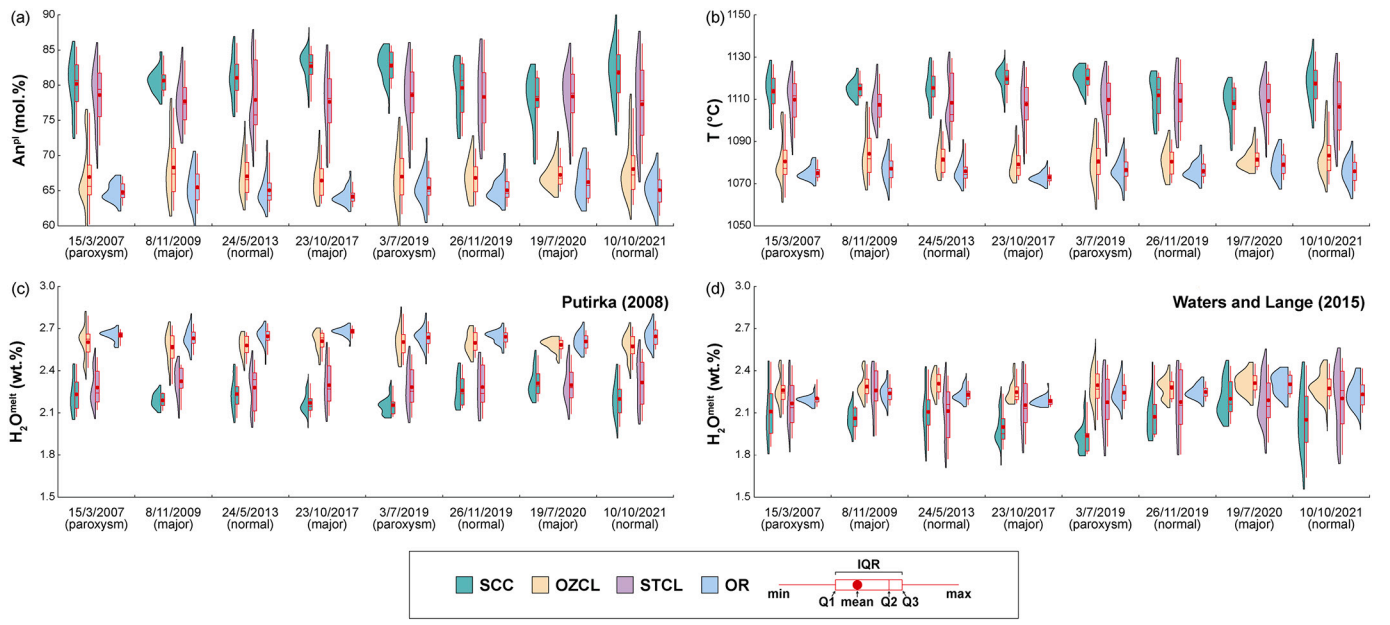

Fig. 11. Violin plots and box plots for anorthite in plagioclase phenocrysts from 2007 to 2021 eruptions at Stromboli (a), temperature predicted by Eq. (44) from this study (b), and melt-water content predicted by the hygrometers of Putirka (2008) (c) and Waters and Lange (2015) (d). A kernel density estimation is used to visualize the underlying probability density function of each set of data in violin plots, whereas the statistical dispersion of data is illustrated by the box plot. The width of the box represents the interquartile range (*IQR*) extending from the first quartile (25th percentile *Q1*) to the third quartile (75th percentile *Q3*) and whiskers go from each quartile to the minimum or maximum. SCC, subrounded corroded cores. STCL, sieve-textured concentric layers. OZCL, oscillatory-zoned concentric layers. OR, overgrowth rims.

the maximum probability distribution of T is 1097–1124 (SCC), 1097–1114 (STCL), 1072–1089 (OZTL), and 1070–1082 (OR) °C (Fig. 11b). In this regard, SCC and STCL reflect high thermal conditions due to inputs of *Lp*-magmas passing through the mush column, OZTL denotes an intermediate cooling stage for magmas residing within the *Hp*-reservoir, and OR likely records the closure temperature of the plagioclase growth at the time of eruption (Di Stefano et al., 2020 and references therein).

For H_2O^{melt} estimated by the hygrometer of Putirka (2008), SCC and STCL box plots are very similar and correspond to melt-water contents lower than those of OZCL and OR box plots (Fig. 11c), in accord with the spatial distribution of An^{pl} (Fig. 11a) and T (Fig. 11b). The maximum probability distribution of H_2O^{melt} is 2.0–2.4 (SCC), 2.1–2.5 (STCL), 2.4–2.8 (OZTL), and 2.5–2.8 (OR) wt% (Fig. 11c). In general, phenocryst zoning patterns return H_2O^{melt} estimates higher than 2 wt% (Fig. 11c), which are very similar to those modeled by La Spina et al. (2015) for the ascent of magma within the crystal mush, but just before rapid microlite crystallization during magma acceleration and abundant volatile exsolution in the uppermost part of the conduit where $H_2O^{melt} \leq 2$ wt% at depth ≤ 1 km. Moreover, the hygrometer of Putirka (2008) records higher amounts of H_2O^{melt} (Fig. 11c) at lower T (Fig. 11b), as the bulk system composition evolves towards lower calcium concentrations in the residual melt and coexisting plagioclase (Fig. 11a) with increasing the degree of crystallization in the colder parts of the mush column. Indeed, as outlined in several works (Armienti et al., 2013; Mollo et al., 2015a; Di Stefano et al., 2020; Palummo et al., 2020), the crystallization of nominally anhydrous minerals (i.e., clinopyroxene and plagioclase) at shallow depths may increase the water content in fluid-undersaturated melts, whereas CaO in the melt and An in plagioclase decrease during magma evolution. The increase of H_2O^{melt} with decreasing both T and An^{pl} corroborates also the thermodynamic principle expressed by Wood and Blundy (2002): for a mineral phase to remain on the liquidus with increasing H_2O^{melt}, the effect of water in lowering the activities of major components must be exactly compensated by an increase of free energy of fusion with decreasing temperature.

On the other hand, for H_2O^{melt} estimated by the hygrometer of Waters and Lange (2015), violin plots and box plots from plagioclase textural domains show less marked differences, with maximum probability distributions of 1.9–2.3 (SCC), 1.9–2.4 (STCL), 2.1–2.4 (OZTL), and 2.1–2.4 (OR) wt% (Fig. 11d). The predictive power of this model is strongly mediated by rival effects between temperature and melt-water content, as a consequence the decrease of H_2O^{melt} (Fig. 11d) with increasing T (Fig. 11b) is attenuated by the increase of An^{pl} (Fig. 11a), and vice versa.

What we learn from the comparative application of the hygrometers of Putirka (2008) and Waters and Lange (2015) is that the two models were calibrated using very different experimental compositions and regression strategies. The model of Putirka (2008) strictly depends on the change of bulk system composition, including An^{pl} and melt major oxides, such that the estimated amount of H_2O^{melt} (Fig. 11c) markedly decreases with increasing T (Fig. 11b). Conversely, less marked hygrometric predictions are obtained by the model of Waters and Lange (2015), as these predictions are more convoluted with compositional-temperature effects controlling the An-Ab exchange reaction. The overriding implication for mafic alkaline magmas is that T and H_2O^{melt} can be simultaneously determined for different plagioclase textural patterns if crystals are sufficiently strongly zoned, and a maximum probability estimation is derived for different textural domains by applying kernel density analysis. However, addition of moderate amounts of water to mafic alkaline melts does not cause substantial modifications for the An-Ab exchange reaction (Fig. 5). As a consequence, hygrometric equations strongly dependent on the equilibrium constant K^{eq}_{An-Ab} appear less sensitive to moderate water changes, as the influence of H_2O^{melt} on An and Ab activities and activity coefficients is mitigated by changes of anhydrous melt components as a function of temperature (cf. §5.2).

7. Conclusions and recommendations

By reviewing natural and experimental plagioclase growth rates from literature and comparing them with new data obtained for mafic alkaline compositions, we document that the temporal scale of

plagioclase morphological evolution is intrinsically related to the change of crystal growth rate upon the effect of interface kinetics. A certain degree of undercooling, leading to melt supersaturation effects, is an essential condition to promote the growth of plagioclase; otherwise, the establishment of a full thermodynamic equilibrium throughout the crystal-melt interface would correspond to a minimum energy state at which the plagioclase growth is halted. According to these kinetic principles, there is a net linear decay of plagioclase growth rate with increasing crystallization time on a logarithmic scale, in response to superimposition of diffusive relaxation phenomena over supersaturation effects at the interface melt. Results from a multifaceted statistical analysis provide that plagioclase growth kinetics can be parameterized under a broad range of isothermal-isobaric and decompression conditions representative of crystallization conditions typically encountered by mafic alkaline magmas at Stromboli and Mt. Etna in Italy. Modeling of crystal size distributions in natural erupted products indicates that degassing-induced microlite crystallization takes place in the order of minutes during fast disequilibrium ascent and acceleration of magma within the conduit. The formation of tiny, elongated plagioclase microlites from explosive eruptions is primarily dictated by fast crystallization kinetics associated with large degrees of undercooling and rapid crystal growth regimes which result from highly dynamic, supersaturated melts. Conversely, large, tabular plagioclase phenocrysts from lava flows grow in response to sluggish kinetic effects associated with small degrees of undercooling and slow crystal growth regimes from more relaxed melts. As a matter of fact, plagioclase phenocrysts within the deeper parts of the plumbing system have more time to grow and equilibrate with the melt upon temporal scales of years.

By reassessing compositional and thermodynamic data from literature, we find that the role of water becomes dominantly important on the control of plagioclase stability and albite-anorthite compositional variability in more differentiated silicic melts, but this effect is evidently less influential for subtle water ranges in mafic alkaline magmas. According to this argument, the predominant effect of temperature on plagioclase saturation is responsible for the weak control of water on melt anorthite and albite activity coefficients as the crystallization of plagioclase proceeds during magma cooling. Different tests carried out on plagioclase-melt compositional data sets from Stromboli provide some practical guidelines that we consider important for future petrological studies. The iterative use of equilibrium, thermometric, and hygrometric equations may represent a secure approach for understanding complex magma dynamics if different textural domains are identified for strongly zoned plagioclase phenocrysts. Owing to error propagation effects resulting from the integration of different modeling equations into a single algorithm, the use of probability-based criteria is essential to correctly disambiguate the role of temperature and melt-water content on plagioclase growth history. The interpretation of iterative modeling data depends on the perception that well categorized plagioclase textures herald specific physico-chemical conditions related to the crystallization of magma. Therefore, error propagation issues can be circumvented through kernel density analysis in which temperature and melt-water contents are first predicted for different plagioclase textural domains and then evaluated as maximum probability distributions.

As an ultimate recommendation, we would caution against using plagioclase and melt compositions that are not tested for equilibrium and may potentially lead to imprecise estimates. Plagioclase-melt equilibrium should be always verified using as many different methods as permitted by the sample data set. A side effect of such approach is the minimization of disequilibrium effects controlling the growth of plagioclase upon magma mixing and ascent dynamics, thus bounding the petrological predictions to isochemical, isobaric, and isothermal conditions. Testing for equilibrium is an essential data-filter attribute for petrological modeling.

Declaration of Competing Interest

The authors declare that they have no known competing financial interests or personal relationships that could have appeared to influence the work reported in this paper.

Data availability

All data are reported as Supllementary Materials

Acknowledgments

Part of this work was supported by Natural Environment research Council UK grant NE/T009292/1 to CMP, INGV Progetti Ricerca Libera 2019 Grant #52/2020 and INGV Departmental Strategic Project UNO to PS, and PRIN MIUR Grant #2017J277S9_004 to AP. For the purpose of open access, CMP has applied a Creative Commons Attribution (CC BY) license to any Author Accepted Manuscript version arising. We are extremely grateful to the thoughtful and constructive comments provided by Keith Putirka, Fabio Arzilli, and two anonymous reviewers. We also thank Arturo Gomez-Tuena for his editorial work.

Appendix A. Supplementary data

Supplementary data to this article can be found online at https://doi.org/10.1016/j.earscirev.2023.104399.

References

Agostini, C., Fortunati, A., Arzilli, F., Landi, P., Carroll, M.R., 2013. Kinetics of crystal evolution as a probe to magmatism at Stromboli (Aeolian Archipelago, Italy). Geochim. Cosmochim. Acta 110, 135–151. https://doi.org/10.1016/j.gca.2013.02.027.

Aigner-Torres, M., Blundy, J., Ulmer, P., Pettke, T., 2007. Laser Ablation ICPMS study of trace element partitioning between plagioclase and basaltic melts: an experimental approach. Contrib. Mineral. Petrol. 153, 647–667. https://doi.org/10.1007/s00410-006-0168-2.

Allard, P., Aiuppa, A., Loyer, H., Carrot, F., Gaudry, A., Pinte, G., Michel, A., Dongarrà, G., 2000. Acid Gas and Metal Emission rates during Long-lived Basalt Degassing at Stromboli Volcano. Geophys. Res. Lett. 27, 1207–1210.

Almeev, R.R., Holtz, F., Koepke, J., Parat, F., 2012. Experimental calibration of the effect of H2O on plagioclase crystallization in basaltic melt at 200 MPa. Am. Mineral. 97, 1234–1240. https://doi.org/10.2138/am.2012.4100.

Aloisi, M., Bonaccorso, A., Gambino, S., 2006. Imaging composite dike propagation (Etna, 2002 case). J. Geophys. Res. 111, B06404. https://doi.org/10.1029/2005JB003908.

Andrews, B.J., 2021. Plagioclase population dynamics and zoning in response to changes in temperature and pressure. Am. Mineral. 106, 1438–1452. https://doi.org/10.2138/am-2021-7491.

Andronico, D., Branca, S., Calvari, S., Burton, M., Caltabiano, T., Corsaro, R.A., Del Carlo, P., Garfì, G., Lodato, L., Miraglia, L., Murè, F., Neri, M., Pecora, E., Pompilio, M., Salerno, G., Spampinato, L., 2005. A multi-disciplinary study of the 2002?03 Etna eruption: insights into a complex plumbing system. Bull. Volcanol. 67, 314–330. https://doi.org/10.1007/s00445-004-0372-8.

Armienti, P., 2008. Decryption of Igneous Rock Textures: Crystal size distribution Tools. Rev. Mineral. Geochem. 69, 623–649.

Armienti, P., Pareschi, M.T., Innocenti, F., Pompilio, M., 1994. Effects of magma storage and ascent on the kinetics of crystal growth: The case of the 1991–93 Mt. Etna eruption. Contrib. Mineral. Petrol. 115, 402–414. https://doi.org/10.1007/BF00320974.

Armienti, P., Pareschi, M.T., Pompilio, M., 1997. Lava textures and time scales of magma storage at Mt. Etna (Italy). Acta Vulcanol. 9, 1–5.

Armienti, P., Perinelli, C., Putirka, K.D., 2013. A New Model to Estimate Deep-level Magma Ascent rates, with applications to Mt. Etna (Sicily, Italy). J. Petrol. 54, 795–813. https://doi.org/10.1093/petrology/egs085.

Arzilli, F., La Spina, G., Burton, M.R., Polacci, M., Le Gall, N., Hartley, M.E., Di Genova, D., Cai, B., Vo, N.T., Bamber, E.C., Nonni, S., Atwood, R., Llewellin, E.W., Brooker, R.A., Mader, H.M., Lee, P.D., 2019. Magma fragmentation in highly explosive basaltic eruptions induced by rapid crystallization. Nat. Geosci. 12, 1023–1028. https://doi.org/10.1038/s41561-019-0468-6.

Bai, L., Baker, D.R., Rivers, M., 2008. Experimental study of bubble growth in Stromboli basalt melts at 1 atm. Earth Planet. Sci. Lett. 267, 533–547.

Barberi, F., Rosi, M., Sodi, A., 1993. Volcanic hazard assessment at Stromboli based on review of histroical data. Acta Vulcanol. 3, 173–187.

Blundy, J., Cashman, K., Humphreys, M., 2006. Magma heating by decompression-driven crystallization beneath andesite volcanoes. Nature 443, 76–80. https://doi.org/10.1038/nature05100.

Botcharnikov, R.E., Almeev, R.R., Koepke, J., Holtz, F., 2008. Phase Relations and liquid Lines of Descent in Hydrous Ferrobasalt-Implications for the Skaergaard Intrusion and Columbia River Flood Basalts. J. Petrol. 49, 1687–1727. https://doi.org/10.1093/petrology/egn043.

Bottinga, Y., Weill, D.F., 1972. The viscosity of magmatic silicate liquids; a model calculation. Am. J. Sci. 272, 438. https://doi.org/10.2475/ajs.272.5.438.

Brugger, C.R., Hammer, J.E., 2010. Crystallization Kinetics in Continuous Decompression experiments: Implications for Interpreting Natural Magma Ascent Processes. J. Petrol. 51, 1941–1965. https://doi.org/10.1093/petrology/egq044.

Burkhard, D.J.M., 2002. Kinetics of crystallization: example of micro-crystallization in basalt lava. Contrib. Mineral. Petrol. 142, 724–737. https://doi.org/10.1007/s00410-001-0321-x.

Burkhard, D.J.M., 2005. Relation between oxidation/crystallization and degassing upon reheating of basalt glass from Kilauea, Hawaii. Mineral. Mag. 69, 103–117. https://doi.org/10.1180/0026461056920238.

Burkhard, D.J.M., 2005b. Nucleation and growth rates of pyroxene, plagioclase, and Fe-Ti oxides in basalt under atmospheric conditions. Eur. J. Mineral. 17, 675–686. https://doi.org/10.1127/0935-1221/2005/0017-0675.

Burnham, C.W., 1975. Water and magmas; a mixing model. Geochim. Cosmochim. Acta 39, 1077–1084.

Carmichael, I.S.E., Nicholls, J., Spera, F.J., Wood, B.J., Nelson, S.A., 1977. High-temperature properties of silicate liquids: applications to the equilibration and ascent of basic magma. Philos. Trans. Royal. Soc. A 286, 373–431. https://doi.org/10.1098/rsta.1977.0124.

Carpenter, M.A., 1988. Thermochemistry of Aluminium/Silicon Ordering in Feldspar Minerals. In: Salje, E.K.H. (Ed.), Physical Properties and Thermodynamic Behaviour of Minerals. Springer, Netherlands, Dordrecht, pp. 265–323. https://doi.org/10.1007/978-94-009-2891-6_9.

Cashman, K., Blundy, J., 2013. Petrological cannibalism: the chemical and textural consequences of incremental magma body growth. Contrib. Mineral. Petrol. 166, 703–729. https://doi.org/10.1007/s00410-013-0895-0.

Cashman, K.V., 1993. Relationship between plagioclase crystallization and cooling rate in basaltic melts. Contrib. Mineral. Petrol. 113, 126–142. https://doi.org/10.1007/BF00320836.

Cashman, K.V., 1990. Textural constraints on the kinetics of crystallization of igneous rocks. Rev. Mineral. Geochem. 24, 259–314.

Cashman, K.V., Marsh, B.D., 1988. Crystal size distribution (CSD) in rocks and the kinetics and dynamics of crystallization II: Makaopuhi lava lake. Contrib. Mineral. Petrol. 99, 292–305. https://doi.org/10.1007/BF00375363.

Cashman, K.V., Thornber, C., Kauahikaua, J.P., 1999. Cooling and crystallization of lava in open channels, and the transition of Pāhoehoe Lava to ʼA'ā. Bull. Volcanol. 61, 306–323. https://doi.org/10.1007/s004450050299.

Cassidy, M., Castro, J.M., Helo, C., Troll, V.R., Deegan, F.M., Muir, D., Neave, D.A., Mueller, S.P., 2016. Volatile dilution during magma injections and implications for volcano explosivity. Geology 44, 1027–1030. https://doi.org/10.1130/G38411.1.

Cassidy, M., Manga, M., Cashman, K., Bachmann, O., 2018. Controls on explosive-effusive volcanic eruption styles. Nat. Commun. 9, 2839. https://doi.org/10.1038/s41467-018-05293-3.

Clocchiatti, R., 1981. La transition augite-diopside et les liquides silicatés intra-cristallins dans les pyroclastes de l'activité actuelle du Stromboli: témoignages de la réinjection et du mélange magmatiques. Bull. Volcanol. 44, 339–357. https://doi.org/10.1007/BF02600569.

Conte, A.M., Perinelli, C., Trigila, R., 2006. Cooling kinetics experiments on different Stromboli lavas: Effects on crystal morphologies and phases composition. J. Volcanol. Geotherm. Res. 155, 179–200. https://doi.org/10.1016/j.jvolgeores.2006.03.025.

Corrigan, G.M., 1982. Supercooling and the crystallization of plagioclase, olivine, and clinopyroxene from basaltic magmas. Mineral. Mag. 46, 31–42. https://doi.org/10.1180/minmag.1982.046.338.06.

Corsaro, R.A., Civetta, L., Di Renzo, V., Miraglia, L., 2009. Petrology of lavas from the 2004–2005 flank eruption of Mt. Etna, Italy: inferences on the dynamics of magma in the shallow plumbing system. Bull. Volcanol. 71, 781–793. https://doi.org/10.1007/s00445-009-0264-z.

Couch, S., 2003. Experimental investigation of crystallization kinetics in a haplogranite system. Am. Mineral. 88, 1471–1485. https://doi.org/10.2138/am-2003-1011.

Couch, S., Sparks, R.S.J., Carroll, M.R., 2001. Mineral disequilibrium in lavas explained by convective self-mixing in open magma chambers. Nature 411, 1037–1039. https://doi.org/10.1038/35082540.

Couch, S., Sparks, R.S.J., Carroll, M.R., 2003. The Kinetics of Degassing-Induced Crystallization at Soufrière Hills Volcano, Montserrat. J. Petrol. 44, 1477–1502.

Crabtree, S.M., Lange, R.A., 2011. Complex Phenocryst Textures and Zoning patterns in Andesites and Dacites: evidence of Degassing-Induced Rapid Crystallization? J. Petrol. 52, 3–38. https://doi.org/10.1093/petrology/egq067.

Del Gaudio, P., Mollo, S., Ventura, G., Iezzi, G., Taddeucci, J., Cavallo, A., 2010. Cooling rate-induced differentiation in anhydrous and hydrous basalts at 500 MPa: implications for the storage and transport of magmas in dikes. Chem. Geol. 270, 164–178.

Di Fiore, F., Vona, A., Kolzenburg, S., Mollo, S., Romano, C., 2021. An Extended Rheological Map of Pāhoehoe—'A'ā transition. JGR Solid Earth 126. https://doi.org/10.1029/2021JB022035.

Di Genova, D., Sicola, S., Romano, C., Vona, A., Fanara, S., Spina, L., 2017. Effect of iron and nanolites on Raman spectra of volcanic glasses: a reassessment of existing strategies to estimate the water content. Chem. Geol. 475, 76–86. https://doi.org/10.1016/j.chemgeo.2017.10.035.

Di Stefano, F., Mollo, S., Ubide, T., Petrone, C.M., Caulfield, J., Scarlato, P., Nazzari, M., Andronico, D., Del Bello, E., 2020. Mush cannibalism and disruption recorded by clinopyroxene phenocrysts at Stromboli volcano: New insights from recent 2003–2017 activity. Lithos 360–361, 105440. https://doi.org/10.1016/j.lithos.2020.105440.

Dohmen, R., Blundy, J., 2014. A predictive thermodynamic model for element partitioning between plagioclase and melt as a function of pressure, temperature and composition. Am. J. Sci. 314, 1319–1372. https://doi.org/10.2475/09.2014.04.

Dowty, E., 1980. Crystal growth and nucleation theory and the numerical simulation of igneous crystallization. In: Hargraves, R.B. (Ed.), The Physics of Magmatic Processes. Princeton University Press, Princeton, New Jersey, USA, pp. 419–485.

Fenn, P.M., 1977. The nucleation and growth of alkali feldspar from hydrous melts. Can. Mineral. 15 (2), 135–161.

Fornaciai, A., Landi, P., Armienti, P., 2009. Dissolution/crystallization kinetics recorded in the 2002–2003 lavas of Stromboli (Italy). Bull. Volcanol. 71, 631–641. https://doi.org/10.1007/s00445-008-0249-3.

Francalanci, L., Davies, G.R., Lustenhouwer, W., Tommasini, S., Mason, P.R.D., Conticelli, S., 2005. Intra-Grain Sr Isotope evidence for Crystal Recycling and Multiple Magma Reservoirs in the recent activity of Stromboli Volcano, Southern Italy. J. Petrol. 46, 1997–2021. https://doi.org/10.1093/petrology/egi045.

Francalanci, L., Avanzinelli, R., Nardini, I., Tiepolo, M., Davidson, J.P., Vannucci, R., 2012. Crystal recycling in the steady-state system of the active Stromboli volcano: a 2.5-ka story inferred from in situ Sr-isotope and trace element data. Contrib. Mineral. Petrol. 163, 109–131. https://doi.org/10.1007/s00410-011-0661-0.

Francalanci, L., Lucchi, F., Keller, J., De Astis, G., Tranne, C.A., 2013. Eruptive, volcano-tectonic and magmatic history of the Stromboli volcano (north-eastern Aeolian archipelago). Geol. Soc. Lond. Mem. 37, 397–471. https://doi.org/10.1144/M37.13.

Gaetani, G.A., Grove, T.L., 1998. The influence of water on melting of mantle peridotite. Contrib. Mineral. Petrol. 131, 323–346.

Ghiorso, M.S., Carmichael, I.S.E., 1980. A regular solution model for met-aluminous silicate liquids: applications to geothermometry, immiscibility, and the source regions of basic magmas. Contrib. Mineral. Petrol. 71, 323–342. https://doi.org/10.1007/BF00374706.

Ghiorso, M.S., Carmichael, I.S.E., Rivers, M.L., Sack, R.O., 1983. The Gibbs free energy of mixing of natural silicate liquids; an expanded regular solution approximation for the calculation of magmatic intensive variables. Contrib. Mineral. Petrol. 84, 107–145. https://doi.org/10.1007/BF00371280.

Giacomoni, P.P., Coltorti, M., Mollo, S., Ferlito, C., Braiato, M., Scarlato, P., 2018. The 2011–2012 paroxysmal eruptions at Mt. Etna volcano: Insights on the vertically zoned plumbing system. J. Volcanol. Geotherm. Res. 349, 370–391. https://doi.org/10.1016/j.jvolgeores.2017.11.023.

Giacomoni, P.P., Ferlito, C., Coltorti, M., Bonadiman, C., Lanzafame, G., 2014. Plagioclase as archive of magma ascent dynamics on "open conduit" volcanoes: The 2001–2006 eruptive period at Mt. Etna. Earth Sci. Rev. 138, 371–393. https://doi.org/10.1016/j.earscirev.2014.06.009.

Ginibre, C., Wörner, G., 2007. Variable parent magmas and recharge regimes of the Parinacota magma system (N. Chile) revealed by Fe, Mg and Sr zoning in plagioclase. Lithos 98, 118–140. https://doi.org/10.1016/j.lithos.2007.03.004.

Giuliani, L., Iezzi, G., Vetere, F., Behrens, H., Mollo, S., Cauti, F., Ventura, G., Scarlato, P., 2020. Evolution of textures, crystal size distributions and growth rates of plagioclase, clinopyroxene and spinel crystallized at variable cooling rates from a mid-ocean ridge basaltic melt. Earth Sci. Rev. 204, 103165 https://doi.org/10.1016/j.earscirev.2020.103165.

Glazner, A.F., 1984. Activities of olivine and plagioclase components in silicate melts and their application to geothermometry. Contrib. Mineral. Petrol. 88, 260–268. https://doi.org/10.1007/BF00380170.

Grove, T.L., 1978. Cooling histories of Luna 24 very low Ti (VLT) ferrobasalts: an experimental study. Proc. Lunar Planet. Sci. Conf. 9th, 565–584.

Grove, T.L., 1990. Cooling histories of lavas from Serocki Volcano. In: Detrick, R., Honnorez, J., Bryan, W.B., Juteau, T. (Eds.), Proc. ODP, Sci. Results, 106/109: College Station, TX (Ocean Drilling Program), pp. 3–8. https://doi.org/10.2973/odp.proc.sr.106109.113.1990.

Gualda, G.A.R., Ghiorso, M.S., Lemons, R.V., Carley, T.L., 2012. Rhyolite-MELTS: a modified calibration of MELTS optimized for silica-rich, fluid-bearing magmatic systems. J. Petrol. 53, 875–890.

Hammer, J.E., 2008. Experimental Studies of the Kinetics and Energetics of Magma Crystallization. Rev. Mineral. Geochem. 69, 9–59. https://doi.org/10.2138/rmg.2008.69.2.

Hammer, J.E., Rutherford, M.J., 2002. An experimental study of the kinetics of decompression-induced crystallization in silicic melt. J. Geophys. Res. 107 https://doi.org/10.1029/2001JB000281. ECV 8-1-ECV 8-24.

Hair, J.F., Anderson, R.E., Tatham, R.L., Black, W.C., 1995. Multivariate Data Analysis. Prentice-Hall, Englewood Cliffs, NJ.

Harris, R.R., Kanji, G.K., 1983. On the use of Minimum Chi-Square Estimation. The Statistician 32, 379–394. https://doi.org/10.2307/2987540.

Higgins, M.D., 2000. Measurement of crystal size distributions. Am. Mineral. 85, 1105–1116.

Housh, T.B., Luhr, J.F., 1991. Plagioclase-melt equilibria in hydrous systems. Am. Mineral. 76, 477–492.

Huggins, E.G., Ruprecht, P., Ghiorso, M.S., 2021. Using Chemical Affinities to Understand Disequilibrium Textures of Plagioclase Preserved in Magmatic Systems. Geophys. Res. Lett. 48 https://doi.org/10.1029/2021GL092884.

Humphreys, M.C.S., Edmonds, M., Klöcking, M.S., 2016. The validity of plagioclase-melt geothermometry for degassing-driven magma crystallization. Am. Mineral. 101, 769–779. https://doi.org/10.2138/am-2016-5314.

Iezzi, G., Mollo, S., Torresi, G., Ventura, G., Cavallo, A., Scarlato, P., 2011. Experimental solidification of an andesitic melt by cooling. Chem. Geol. 283, 261–273. https://doi.org/10.1016/j.chemgeo.2011.01.024.

Iezzi, G., Mollo, S., Shahini, E., Cavallo, A., Scarlato, P., 2014. The cooling kinetics of plagioclase feldspar as revealed by electron-microprobe mapping. Am. Mineral. 99, 898–907.
Ikeda, Y., 1977. Grain size of plagioclase of the basaltic andesite dikes, Iritono, central Abukuma plateau. Can. J. Earth Sci. 14, 1860–1866. https://doi.org/10.1139/e77-157.
Ishibashi, H., 2013. Spinel-melt oxygen barometry; a method and application to Cenozoic alkali basaltic magmas from the Higashi-Matsuura District, NW Kyushu, Japan. Geosci. Rep. Shizuoka Univ. 40, 21–32.
Jackson, K., 1969. Current concepts in crystal growth: the fundamental rate equation. J. Crystal Growth 5, 13–18.
James, O.B., McGee, J.J., 1992. Compositional variations in mare-basalt plagioclase produced by differing crystallization regimes. Lunar Planet. Sci. XXIII, 603–604 (abstr.).
Kirkpatrick, R.J., Klein, L., Uhlmann, D.R., Hays, J.F., 1979. Rates and processes of crystal growth in the system anorthite-albite. J. Geophys. Res. 84, 3671–3676. https://doi.org/10.1029/JB084iB07p03671.
Kirkpatrick, R.J., 1975. Crystal Growth from the Melt: a Review. Am. Mineral. 60, 798–814.
Kirkpatrick, R.J., 1981. Kinetics of crystallization of igneous rocks. In: Lasaga, A.C., Kirkpatrick, R.J. (Eds.), Rev Mineral Geochem, 8, pp. 321–397.
Kirkpatrick, R.J., Kuo, L.C., 1981. Crystal growth in incongruently-melting compositions: programmed cooling experiments with diopside. Am. Mineral. 66, 223–241.
Kirkpatrick, R.J., 1983. Theory of nucleation in silicate melts. Am. Mineral. 68, 66–77.
Kneedler, A.E., 1989. Quantitative petrographic study of two diabase dikes intruded into the Sao Francisco craton, brasil. Princeton University. BA Thesis.
Kohut, E., Nielsen, R.L., 2004. Melt inclusion formation mechanisms and compositional effects in high-an feldspar and high-Fo olivine in anhydrous mafic silicate liquids. Contrib. Mineral. Petrol. 147, 684–704. https://doi.org/10.1007/s00410-004-0576-0.
Kouchi, A., Tsuchiyama, A., Sunagawa, I., 1986. Effect of stirring on crystallization kinetics of basalt: texture and element partitioning. Contrib. Mineral. Petrol. 93, 429–438.
Kress, V.C., Carmichael, I.S.E., 1988. Stoichiometry of the iron oxidation reaction in silicate melts. Am. Mineral. 73, 1267–1274.
Kress, V.C., Carmichael, I.S.E., 1991. The compressibility of silicate liquids containing Fe2O3 and the effect of composition, temperature, oxygen fugacity and pressure on their redox states. Contrib. Mineral. Petrol. 108, 82–92.
La Spina, G., Burton, M., Michieli Vitturi, M., 2015. Temperature evolution during magma ascent in basaltic effusive eruptions: a numerical application to Stromboli volcano. Earth Planet. Sci. Lett. 426, 89–100. https://doi.org/10.1016/j.epsl.2015.06.015.
La Spina, G., Burton, M., Michieli Vitturi, M., Arzilli, F., 2016. Role of syn-eruptive plagioclase disequilibrium crystallization in basaltic magma ascent dynamics. Nat. Commun. 7, 13402. https://doi.org/10.1038/ncomms13402.
La Spina, G., Arzilli, F., Llewellin, E.W., Burton, M.R., Clarke, A.B., Michieli Vitturi, M., Polacci, M., Hartley, M.E., Di Genova, D., Mader, H.M., 2021. Explosivity of basaltic lava fountains is controlled by magma rheology, ascent rate and outgassing. Earth Planet. Sci. Lett. 553, 116658 https://doi.org/10.1016/j.epsl.2020.116658.
Landi, P., Métrich, N., Bertagnini, A., Rosi, M., 2004. Dynamics of magma mixing and degassing recorded in plagioclase at Stromboli (Aeolian Archipelago, Italy). Contrib. Mineral. Petrol. 147, 213–227. https://doi.org/10.1007/s00410-004-0555-5.
Landi, P., Francalanci, L., Pompilio, M., Rosi, M., Corsaro, R.A., Petrone, C.M., Nardini, I., Miraglia, L., 2006. The December 2002–July 2003 effusive event at Stromboli volcano, Italy: Insights into the shallow plumbing system by petrochemical studies. J. Volcanol. Geotherm. Res. 155, 263–284. https://doi.org/10.1016/j.jvolgeores.2006.03.032.
Larsen, J.F., 2005. Experimental study of plagioclase rim growth around anorthite seed crystals in rhyodacitic melt. Am. Mineral. 90, 417–427. https://doi.org/10.2138/am.2005.1456.
Lasaga, A.C., 1998. In: Kinetic Theory in the Earth Sciences. Princeton Univ. Press, Princeton, NJ, p. 781.
Lang, S., Mollo, S., France, L., Misiti, V., Nazzari, M., 2021. Kinetic partitioning of major-minor cations between olivine and hawaiian tholeiitic basalt under variable undercooling and cooling rate conditions. Chem. Geol. 584, 120485 https://doi.org/10.1016/j.chemgeo.2021.120485.
Lange, R.A., Frey, H.M., Hector, J., 2009. A thermodynamic model for the plagioclase-liquid hygrometer/thermometer. Am. Mineral. 94, 494–506. https://doi.org/10.2138/am.2009.3011.
Le Gall, N., Arzilli, F., La Spina, G., Polacci, M., Cai, B., Hartley, M.E., Vo, N.T., Atwood, R.C., Di Genova, D., Nonni, S., Llewellin, E.W., Burton, M.R., Lee, P.D., 2021. In situ quantification of crystallisation kinetics of plagioclase and clinopyroxene in basaltic magma: Implications for lava flow. Earth Planet. Sci. Lett. 568, 117016 https://doi.org/10.1016/j.epsl.2021.117016.
Lindsley, D.H., Smith, D., 1971. Chemical variations in the feldspars. In: Carnegie Institute of Washington Yearb, 69, pp. 274–278.
Lofgren, G., 1974. An experimental study of plagioclase crystal morphology; isothermal crystallization. Am. J. Sci. 274, 243–273. https://doi.org/10.2475/ajs.274.3.243.
Lofgren, G., 1980. Experimental studies on the dynamic crystallization of silicate melts. In: Hargraves, R.B. (Ed.), The Physics of Magmatic Processes. Princeton University Press, Princeton, pp. 487–551.
Long, D.A., 1977. In: Raman Spectroscopy. McGraw-Hill, p. 276.
Longhi, J., Walker, D., Hays, J.F., 1976. Fe and Mg in plagioclase. Proc. Lunar Sci. Conf. 7th, 1281–1300.
Marsh, B.D., 1988. Crystal size distribution (CSD) in rocks and the kinetics and dynamics of crystallization. Contrib. Mineral. Petrol. 99, 277–291.
Masotta, M., Mollo, S., Freda, C., Gaeta, M., Moore, G., 2013. Clinopyroxene–liquid thermometers and barometers specific to alkaline differentiated magmas. Contrib. Mineral. Petrol. 166, 1545–1561. https://doi.org/10.1007/s00410-013-0927-9.
Métrich, N., Rutherford, M.J., 1998. Low pressure Crystallization Paths of H2O-saturated Basaltic-Hawaiitic Melts from Mt Etna: Implications for Open-System Degassing of Basaltic Volcanoes. Geochim. Cosmochim. Acta 62, 1195–1205. https://doi.org/10.1016/S0016-7037(98)00048-9.
Métrich, N., Allard, P., Spilliaert, N., Andronico, D., Burton, M., 2004. 2001 flank eruption of the alkali- and volatile-rich primitive basalt responsible for Mount Etna's evolution in the last three decades. Earth Planet. Sci. Lett. 228, 1–17. https://doi.org/10.1016/j.epsl.2004.09.036.
Métrich, N., Bertagnini, A., Di Muro, A., 2010. Conditions of Magma Storage, Degassing and Ascent at Stromboli: New Insights into the Volcano Plumbing System with Inferences on the Eruptive Dynamics. J. Petrol. 51, 603–626. https://doi.org/10.1093/petrology/egp083.
Mollard, E., Martel, C., Bourdier, J.-L., 2012. Decompression-induced Crystallization in Hydrated Silica-rich Melts: Empirical Models of Experimental Plagioclase Nucleation and Growth Kinetics. J. Petrol. 53, 1743–1766. https://doi.org/10.1093/petrology/egs031.
Mollo, S., Putirka, K., Iezzi, G., Del Gaudio, P., Scarlato, P., 2011. Plagioclase–melt (dis) equilibrium due to cooling dynamics: Implications for thermometry, barometry and hygrometry. Lithos 125, 221–235. https://doi.org/10.1016/j.lithos.2011.02.008.
Mollo, S., Misiti, V., Scarlato, P., Soligo, M., 2012. The role of cooling rate in the origin of high temperature phases at the chilled margin of magmatic intrusions. Chem. Geol. 322–323, 28–46. https://doi.org/10.1016/j.chemgeo.2012.05.029.
Mollo, S., Putirka, K., Misiti, V., Soligo, M., Scarlato, P., 2013. A new test for equilibrium based on clinopyroxene–melt pairs: Clues on the solidification temperatures of Etnean alkaline melts at post-eruptive conditions. Chem. Geol. 352, 92–100. https://doi.org/10.1016/j.chemgeo.2013.05.026.
Mollo, S., Giacomoni, P.P., Coltorti, M., Ferlito, C., Iezzi, G., Scarlato, P., 2015a. Reconstruction of magmatic variables governing recent Etnean eruptions: Constraints from mineral chemistry and P-T–fO2–H2O modeling. Lithos 212–215, 311–320. https://doi.org/10.1016/j.lithos.2014.11.020.
Mollo, S., Giacomoni, P.P., Andronico, D., Scarlato, P., 2015b. Clinopyroxene and titanomagnetite cation redistributions at Mt. Etna volcano (Sicily, Italy): Footprints of the final solidification history of lava fountains and lava flows. Chem. Geol. 406, 45–54. https://doi.org/10.1016/j.chemgeo.2015.04.017.
Mollo, S., Masotta, M., Forni, F., Bachmann, O., De Astis, G., Moore, G., Scarlato, P., 2015c. A K-feldspar-liquid hygrometer specific to alkaline differentiated magmas. Chem. Geol. 392, 1–8. https://doi.org/10.1016/j.chemgeo.2014.11.010.
Mollo, S., Vetere, F., Beherens, H., Tecchiato, V., Langone, A., Scarlato, P., Perugini, D., 2017. The effect of degassing and volatile exsolution on the composition of a trachybasaltic melt decompressed at slow and fast rates. Period. Mineral. 86 https://doi.org/10.2451/2017PM691.
Mollo, S., Hammer, J.E., 2017. Dynamic crystallization in magmas. In: Heinrich, W., Abart, R. (Eds.), Mineral Reaction Kinetics: Microstructures, Textures, Chemical and Isotopic Signatures. Mineralogical Society of Great Britain & Ireland, pp. 378–418. https://doi.org/10.1180/EMU-notes.16.12.
Mollo, S., Blundy, J., Scarlato, P., De Cristofaro, S.P., Tecchiato, V., Di Stefano, F., Vetere, F., Holtz, F., Bachmann, O., 2018. An integrated P-T-H2O-lattice strain model to quantify the role of clinopyroxene fractionation on REE+Y and HFSE patterns of mafic alkaline magmas: Application to eruptions at Mt. Etna. Earth Sci. Rev. 185, 32–56. https://doi.org/10.1016/j.earscirev.2018.05.014.
Moore, J.G., Evans, B.W., 1967. The role of olivine in the crystallization of the prehistoric Makaopuhi tholeiitic lava lake, Hawaii. Contrib. Mineral. Petrol. 15, 202–223. https://doi.org/10.1007/BF01185342.
Morgan, D.J., Jerram, D.A., 2006. On estimating crystal shape for crystal size distribution analysis. J. Volcanol. Geotherm. Res. 154, 1–7. https://doi.org/10.1016/j.jvolgeores.2005.09.016.
Moschini, P., Mollo, S., Gaeta, M., Fanara, S., Nazzari, M., Petrone, C.M., Scarlato, P., 2021. Parameterization of clinopyroxene growth kinetics via crystal size distribution (CSD) analysis: Insights into the temporal scales of magma dynamics at Mt. Etna volcano. Lithos 396–397, 106225. https://doi.org/10.1016/j.lithos.2021.106225.
Muncill, G.E., Lasaga, A.C., 1987. Crystal-growth kinetics of plagioclase in igneous systems: One-atmosphere experiments and application of a simplified growth model. Am. Mineral. 72, 299–311.
Muncill, G.E., Lasaga, A.C., 1988. Crystal-growth kinetics of plagioclase in igneous systems: Isothermal H2O-saturated experiments and extension of a growth model to complex silicate melts. Am. Mineral. 73, 982–992.
Mysen, B.O., Carmichael, I.S.E., Virgo, D., 1985. A comparison of iron redox ratios in silicate glasses determined by wet-chemical and 57 Fe Mössbauer resonant absorption methods. Contrib. Mineral. Petrol. 90, 101–106.
Nabelek, P.I., Taylor, L.A., Lofgren, G.E., 1978. Nucleation and growth of plagioclase and the development of textures in a high-alumina basaltic melt. Proc. Lunar Planet. Sci. Conf. 9th, 725–741.
Namur, O., Charlier, B., Toplis, M.J., Vander Auwera, J.V., 2012. Prediction of plagioclase-melt equilibria in anhydrous silicate melts at 1-atm. Contrib. Mineral. Petrol. 163, 133–150. https://doi.org/10.1007/s00410-011-0662-z.
Naney, M.T., Swanson, S.E., 1980. The effect of Fe and Mg on crystallization in granitic systems. Am. Mineral. 65, 639–653.
Nelson, S.T., Montana, A., 1992. Sieve-textured plagioclase in volcanic rocks produced by rapid decompression. Am. Mineral. 77, 1242–1249.
Nicholls, J., 1980. A simple Thermodynamic Model for estimating the Solubility of H2O in Magmas. Contrib. Mineral. Petrol. 74, 211–220.
Nielsen, R.L., Drake, M.J., 1979. Pyroxene-melt equilibria. Geochim. Cosmochim. Acta 43, 1259–1272. https://doi.org/10.1016/0016-7037(79)90117-0.

Orlando, A., D'Orazio, M., Armienti, P., Borrini, D., 2008. Experimental determination of plagioclase and clinopyroxene crystal growth rates in an anhydrous trachybasalt from Mt Etna (Italy). Eur. J. Mineral. 20, 653–664. https://doi.org/10.1127/0935-1221/2008/0020-1841.

Palummo, F., Mollo, S., De Astis, G., Di Stefano, F., Nazzari, M., Scarlato, P., 2020. Petrological and geochemical modeling of magmas erupted at Vulcano Island in the period 54–8 ka: Quantitative constraints on the sub-volcanic architecture of the plumbing system. Lithos 374–375, 105715.

Perinelli, C., Mollo, S., Gaeta, M., De Cristofaro, S.P., Palladino, D.M., Armienti, P., Scarlato, P., Putirka, K.D., 2016. An improved clinopyroxene-based hygrometer for Etnean magmas and implications for eruption triggering mechanisms. Am. Mineral. 101, 2774–2777. https://doi.org/10.2138/am-2016-5916.

Peters, M.T., Shaffer, E.E., Burnett, D.S., Kim, S.S., 1995. Magnesium and titanium partitioning between anorthite and Type B CAI liquid: Dependence on oxygen fugacity and liquid composition. Geochim. Cosmochim. Acta 59, 2785–2796. https://doi.org/10.1016/0016-7037(95)00173-W.

Petrone, C.M., Bugatti, G., Braschi, E., Tommasini, S., 2016. Pre-eruptive magmatic processes re-timed using a non-isothermal approach to magma chamber dynamics. Nat. Commun. 7, 12946.

Petrone, C.M., Braschi, E., Francalanci, L., Casalini, M., Tommasini, S., 2018. Rapid mixing and short storage timescale in the magma dynamics of a steady-state volcano. Earth Planet. Sci. Lett. 492, 206–221.

Petrone, C.M., Mollo, S., Gertisser, R., Buret, Y., Scarlato, P., Del Bello, E., Andronico, D., Ellis, B., Pontesilli, A., De Astis, G., Giacomoni, P., Coltorti, M., Reagan, M., 2022. 2022, Magma recharge and mush rejuvenation drive paroxysmal activity at Stromboli volcano. Nat. Commun. 13, 7717.

Phinney, W.C., 1992. Partition coefficients for iron between plagioclase and basalt as a function of oxygen fugacity: Implications for Archean and lunar anorthosites. Geochim. Cosmochim. Acta 56, 1885–1895. https://doi.org/10.1016/0016-7037(92)90318-D.

Polacci, M., Andronico, D., Michieli Vitturi, M., Taddeucci, J., Cristaldi, A., 2019. Mechanisms of Ash Generation at Basaltic Volcanoes: The Case of Mount Etna, Italy. Front. Earth Sci. 7, 193. https://doi.org/10.3389/feart.2019.00193.

Pontesilli, A., Masotta, M., Nazzari, M., Mollo, S., Armienti, P., Scarlato, P., Brenna, M., 2019. Crystallization kinetics of clinopyroxene and titanomagnetite growing from a trachybasaltic melt: New insights from isothermal time-series experiments. Chem. Geol. 510, 113–129. https://doi.org/10.1016/j.chemgeo.2019.02.015.

Pontesilli, A., Brenna, M., Ubide, T., Mollo, S., Masotta, M., Caulfield, J., Le Roux, P., Nazzari, M., Scott, J.M., Scarlato, P., 2021. Intraplate Basalt Alkalinity Modulated by a Lithospheric Mantle Filter at the Dunedin Volcano (New Zealand). J. Petrol. 62 (10) https://doi.org/10.1093/petrology/egab062.

Pupier, E., Duchene, S., Toplis, M.J., 2008. Experimental quantification of plagioclase crystal size distribution during cooling of a basaltic liquid. Contrib. Mineral. Petrol. 155, 555–570. https://doi.org/10.1007/s00410-007-0258-9.

Putirka, K.D., 2005. Igneous thermometers and barometers based on plagioclase + liquid equilibria: Tests of some existing models and new calibrations. Am. Mineral. 90, 336–346. https://doi.org/10.2138/am.2005.1449.

Putirka, K.D., 2008. Thermometers and Barometers for Volcanic Systems. Rev. Mineral. Geochem. 69 (1), 61–120. https://doi.org/10.2138/rmg.2008.69.3.

Putirka, K.D., 2017. Geothermometry and Geobarometry. In: White, W. (Ed.), Encyclopedia of Geochemistry. Encycl. Earth Sci. Ser. Springer, Cham. https://doi.org/10.1007/978-3-319-39193-9_322-1.

Putirka, K.D., Johnson, M., Kinzler, R., Longhi, J., Walker, D., 1996. Thermobarometry of mafic igneous rocks based on clinopyroxene-liquid equilibria, 0–30 kbar. Contrib. Mineral. Petrol. 123, 92–108. https://doi.org/10.1007/s004100050145.

Sato, H., 1989. Mg-Fe partitioning between plagioclase and liquid in basalts of hole 504B, ODP LEG 111: A study of melting at 1 atm. In: Proceedings of the Ocean Drilling Program, 111 Scientific Results 111.

Schiavi, F., Walte, N., Keppler, H., 2009. First in situ observation of crystallization processes in a basaltic-andesitic melt with the moissanite cell. Geology 37, 963–966. https://doi.org/10.1130/G30087A.1.

Schiavi, F., Kobayashi, K., Moriguti, T., Nakamura, E., Pompilio, M., Tiepolo, M., Vannucci, R., 2010. Degassing, crystallization and eruption dynamics at Stromboli: trace element and lithium isotopic evidence from 2003 ashes. Contrib. Mineral. Petrol. 159, 541–561. https://doi.org/10.1007/s00410-009-0441-2.

Schanofsky, M., Fanara, S., Schmidt, B.C., 2019. CO2-H2O solubility in K-rich phonolitic and leucititic melts. Contrib. Mineral. Petrol. 174, 52. https://doi.org/10.1007/s00410-019-1581-7.

Shea, T., Hammer, J.E., 2013. Kinetics of cooling- and decompression-induced crystallization in hydrous mafic-intermediate magmas. J. Volcanol. Geotherm. Res. 260, 127–145. https://doi.org/10.1016/j.jvolgeores.2013.04.018.

Shirley, D.N., 1987. Differentiation and Compaction in the Palisades Sill, New Jersey. J. Petrol. 28, 835–865. https://doi.org/10.1093/petrology/28.5.835.

Simakin, A.G., Salova, T.P., 2004. Plagioclase Crystallization from a Hawaiitic Melt in experiments and in a Volcanic Conduit. Petrology 12, 82–92.

Singer, B.S., Pearce, T.H., Kolisnik, A.M., Myers, J.D., 1993. Plagioclase zoning in mid-Pleistocene lavas from the Seguam volcanic center, central Aleutian arc, Alaska. Am. Mineral. 87, 143–157.

Sisson, T.W., Grove, T.L., 1993. Experimental investigations of the role of H2O in calc-alkaline differentiation and subduction zone magmatism. Contrib. Mineral. Petrol. 113, 143–166.

Smith, J.Y., Brown, W.L., 1988. Feldspar minerals vol. I: Crystal structures, physical, chemical, and microtextural properties. In: 2nd edition. Springer, Berlin, Heidelberg New, p. 828.

Smith, J.V., 1974. Feldspar Minerals. Vol. 2: Chemical and Textural Properties. Springer-Verlag., New York.

Smith, R.K., Lofgren, G.E., 1983. An analytical and experimental study of zoning in plagioclase. Lithos 16, 153–168.

Stolper, E., 1982. The speciation of water in silicate melts. Geochim. Cosmochim. Acta 46, 2609–2620. https://doi.org/10.1016/0016-7037(82)90381-7.

Sugawara, T., 2001. Ferric iron partitioning between plagioclase and silicate liquid: thermodynamics and petrological applications. Contrib. Mineral. Petrol. 141, 659–686. https://doi.org/10.1007/s004100100267.

Swanson, S.E., 1977. Relation of nucleation and crystal-growth rate to the development of granitic textures. Am. Mineral. 62, 966–978.

Sun, C., Graff, M., Liang, Y., 2017. Trace element partitioning between plagioclase and silicate melt: the importance of temperature and plagioclase composition, with implications for terrestrial and lunar magmatism. Geochim. Cosmochim. Acta 206, 273–295. https://doi.org/10.1016/j.gca.2017.03.003.

Tsuchiyama, A., 1983. Crystallization kinetics in the system CaMgSi206-CaAI2Si2O8: the delay in nucleation of diopside and anorthite. Am. Mineral. 68, 687–698.

Tsuchiyama, A., 1985. Crystallization kinetics in the system CaMgSi206-CaAI2Si2O8: development of zoning and kinetics effects on element partitioning. Am. Mineral. 70, 474–486.

Ubide, T., Caulfield, J., Brandt, C., Bussweiler, Y., Mollo, S., Di Stefano, F., Nazzari, M., Scarlato, P., 2019. Deep Magma Storage revealed by Multi-Method Elemental Mapping of Clinopyroxene Megacrysts at Stromboli Volcano. Front. Earth Sci. 7, 239.

Ueki, K., Kuwatani, T., Okamoto, A., Akaho, S., Iwamori, H., 2020. Thermodynamic modeling of hydrous-melt–olivine equilibrium using exhaustive variable selection. Phys. Earth Planet. Int. 300, 106430 https://doi.org/10.1016/j.pepi.2020.106430.

Vetere, F., Iezzi, G., Behrens, H., Holtz, F., Ventura, G., Misiti, V., Cavallo, A., Mollo, S., Dietrich, M., 2015. Glass forming ability and crystallisation behaviour of sub-alkaline silicate melts. Earth Sci. Rev. 150, 25–44. https://doi.org/10.1016/j.earscirev.2015.07.001.

Vona, A., Romano, C., 2013. The effects of undercooling and deformation rates on the crystallization kinetics of Stromboli and Etna basalts. Contrib. Mineral. Petrol. 166, 491–509. https://doi.org/10.1007/s00410-013-0887-0.

Waters, L.E., Lange, R.A., 2015. An updated calibration of the plagioclase-liquid hygrometer-thermometer applicable to basalts through rhyolites. Am. Mineral. 100, 2172–2184. https://doi.org/10.2138/am-2015-5232.

Watson, E.B., Müller, T., 2009. Non-equilibrium isotopic and elemental fractionation during diffusion-controlled crystal growth under static and dynamic conditions. Chem. Geol. 267, 111–124. https://doi.org/10.1016/j.chemgeo.2008.10.036.

Wilke, M., Behrens, H., 1999. The dependence of the partitioning of iron and europium between plagioclase and hydrous tonalitic melt on oxygen fugacity. Contrib. Mineral. Petrol. 137, 102–114. https://doi.org/10.1007/s004100050585.

Wood, B.J., Blundy, J.D., 2002. The effect of H2O on crystal-melt partitioning of trace elements. Geochim. Cosmochim. Acta 66, 3647–3656. https://doi.org/10.1016/S0016-7037(02)00935-3.

Wright, T.L., Okamura, R.T., 1977. Cooling and crystallization of tholeiitic basalt, 1965 Makaopuhi lava lake, Hawaii. In: US Geol Surv Prof Pap, p. 1004.

Xue, S., Morse, S.A., 1994. Chemical characteristics of plagioclase and pyroxene megacrysts and their significance to the petrogenesis of the Nain anorthosites. Geochim. Cosmochim. Acta 58, 4317–4331. https://doi.org/10.1016/0016-7037(94)90336-0.

Zhang, Y., 2010. Diffusion in minerals and melts: theoretical background. In: Zhang, Y., Cherniak, D. (Eds.), Diffusion in Minerals and Melts, 72, pp. 5–60. Rev. Mineral. Geochem.